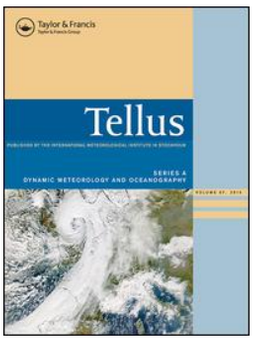

Tellus A: Dynamic Meteorology and Oceanography

ISSN: (Print) 1600-0870 (Online) Journal homepage: https://www.tandfonline.com/loi/zela20

Climatological descriptions on regional circulation around the Korean Peninsula

Eun Ae Lee, Sung Yong Kim & Hong Sik Min

To cite this article: Eun Ae Lee, Sung Yong Kim & Hong Sik Min (2019) Climatological descriptions on regional circulation around the Korean Peninsula, Tellus A: Dynamic Meteorology and Oceanography, 71:1, 1-22, DOI: 10.1080/16000870.2019.1604058

To link to this article: https://doi.org/10.1080/16000870.2019.1604058

Published online: 20 May 2019.

Tellus SERIES A DYANAMIC METEOROLOGY AND OCEANOGRAPHY
PUBLISHED BY THE INTERNATIONAL METEOROLOGICAL INSTITUTE IN STOCKHOLM

Climatological descriptions on regional circulation around the Korean Peninsula

By EUN AE LEE[1], SUNG YONG KIM[1]*, and HONG SIK MIN[2], [1]*Environmental Fluid Mechanics Laboratory, Department of Mechanical Engineering, Korea Advanced Institute of Science and Technology, Daejeon, Republic of Korea;* [2]*Ocean Circulation and Climate Research Center, Korea Institute of Ocean Science and Technology, Busan, Republic of Korea*

(Manuscript received 06 August 2018; in final form 03 April 2019)

ABSTRACT

The coastal ocean climatology of the temperature and salinity around the Korean Peninsula [Yellow Sea (YS), South Sea of Korea (SS), and East/Japan Sea (EJS)] is derived from conductivity-temperature-depth (CTD) profiles, which are collected from historical hydrographic surveys conducted over the last 20 years (1995 to 2014), using a multivariate regression analysis having basis functions of the temporal mean, annual and semiannual cycles, and linear trend. Based on the temporal means of the temperature and salinity profiles, the regional mesoscale circulation is reviewed with regard to the boundary currents, geostrophic currents, and density compensation and layered density structures associated with distinct water properties. The temperature in the YS exhibits a two-layer system, with decreasing annual amplitudes onshore above 25 m and offshore below 25 m because of annually modulated tidal mixing. The annual and semiannual variability in the temperature in the EJS primarily appears in the surface (upper 50 m) and intermediate (between 50 m and 200 m) layers, respectively, because of annual surface heat fluxes and southward subsurface regional currents (e.g. the North Korea Cold Current). For the linear trend in the temperature, the onshore decreasing and offshore increasing tendencies in the EJS are described by the transport of long-term heat contents associated with the regional boundary currents. The multivariate regression analysis presented here explains approximately 90% of the variance in the temperature and salinity in the upper 100 m (corresponding to most of the depths in the YS and SS).

Keywords: annual and semi-annual circulation, uncertainty of regression analysis, linear trend, interannual variability, East/Japan Sea, Yellow Sea. South Sea of Korea

1. Introduction

Fundamental observations in oceanography have been initiated by investigations of seawater properties, such as temperature (T) and salinity (S), at the ocean surface and in the interior (Veronis, 1972; Abraham et al., 2013). The distinct relationships between temperature and salinity have been used to elucidate the ocean circulation and the structure of the upper ocean (Stommel, 1962; Turner and Stommel, 1964). For example, sampled and gridded temperature and salinity data in four-dimensional space (x, y, z, and t) have been used to track the ventilation of deep waters, i.e. thermohaline circulation (Luyten et al., 1993), and their ratios have been uniquely identified in the thermocline and the mixed layer (Rudnick and Ferrari, 1999). The climatology of the global oceanic temperature and salinity at the ocean surface and in the interior has been investigated via long-term hydrographic surveys and oceanographic expeditions, including the World Ocean Circulation Experiment (WOCE) (WOCE International Project Office, 2003; Gouretski and Koltermann, 2004) as well as other periodic surveys (Levitus et al., 1998; Roemmich and Gilson, 2009) (see Hartmann (1994) for more examples), which have provided benefits to both regional circulation studies and fishery science. Regional hydrographic surveys and relevant oceanographic circulation studies have been conducted in various coastal and offshore regions, including the United States (Lynn and Simpson, 1987; Castelao et al., 2010), the European Union (EuroSITES) (Cardin et al., 2010), Australia (Schaeffer et al., 2016), and the Korean Peninsula (Kang and Jin, 1984a; Jeong et al., 2009).

*Corresponding author. e-mail: syongkim@kaist.ac.kr

Citation: Tellus A: 2019, **71**, 1604058, https://doi.org/10.1080/16000870.2019.1604058

The regional circulation around the Korean Peninsula is typically characterized by (1) tide-dominant currents in the Yellow Sea (YS) (Hwang et al., 2014), (2) geostrophic currents and regional boundary currents in the East/Japan Sea (EJS) (Kim et al., 2001), and (3) complex coastal currents associated with these two distinct regional currents in the South Sea of Korea (SS) (Kim et al., 2000; Lie et al., 2015). The complex regional circulation is composed of multiple components, including tidal fronts and tidal currents around islands and coastal boundaries (Lie, 1989; Hwang et al., 2014; Jeong et al., 2009), a regional boundary current of the Tsushima Warm Current (TWC) and its intrusion (Cho and Kim, 1996; Lie et al., 2001), a subpolar front resulting from the confluence of subtropical and subpolar waters in the EJS (Talley et al., 2006; Gordon et al., 2002), thermohaline circulation associated with heat fluxes and salinity gradients (Yoshikawa et al., 1999; Lee et al., 2006), migration of persistent and intermittent fronts over continental shelves (Son et al., 2010; Yang et al., 1998), and annual precipitation and evaporation (Hwang et al., 2014; Lie, 1984) (see Fig. 1a for primary regional currents).

The seasonal circulation around the Korean Peninsula has been described by the northeastward TWC and southward North Korea Cold Current (NKCC) in the EJS, the YS Warm Current (YSWC) and West Korea Coastal Current (WKCC) in the YS, and the migration and propagation of the regional fronts in the SS (Kim and Kim, 1983; Yun et al., 2004; Lie et al., 2001; Pang et al., 2003) (Fig. 1a). In addition, distinct phenomena with nonseasonal (or interannual) variability are observed, including the Ulleung Warm Eddy (UWE), East Sea Intermediate Water (ESIW), and Yellow Sea Bottom Cold Water (YSBCW) (Cho et al., 1990; Kim and Kim, 1999; Hu et al., 1991) (see Table 1 for acronyms of the regional currents).

This paper aims to answer the following three questions: (1) How well do the temporal mean, annual and semiannual variability, and linear trend in the temperature and salinity profiles for the most recent 20 years (1995 to 2014) represent the regional circulation around the Korean Peninsula? (2) How can the derived climatology be applied to regional circulation studies? (3) How can the uncertainty of the regression analysis be quantified? To investigate these three questions, we conduct a multivariate regression analysis using basis functions of the temporal mean, annual and semiannual cycles, and linear trend. Then, we interpret the regression results in the context of the regional circulation. In particular, we have reviewed the literature reporting conductivity-temperature-depth (CTD) observations (partially) during periods that overlap with or are prior to the study time window (1995 to 2014) and providing physical interpretations to highlight the similarities and differences with the regression results in this paper.

This paper is divided into four sections. Hydrographic survey data (temperature and salinity) and the regression analysis are described in Section 2. The temporal mean and variability (standard deviation) of the sampled data, the amplitudes and phases at annual and semiannual frequencies and the linear trend are discussed in Section 3. A discussion and conclusions follow in Sections 4 and 5, respectively. In addition, an extensive uncertainty estimation of the regression analysis is summarized in Appendix A, and this summary extends and improves upon similar multivariate regression analyses studied elsewhere (Kim and Cornuelle, 2015).

2. Data analysis

2.1. Hydrographic survey data

As part of the historical hydrographic surveys performed around the Korean Peninsula beginning in 1961, the temperature and salinity profiles have typically been sampled six times a year since 1994 using a CTD sensor. These surveys were operated by the National Institute of Fisheries Science (NIFS), and the initial quality assurance and quality controlled (QAQC'd) data were distributed via the Korea Oceanographic Data Center (KODC) (Lee et al., 2010). Note that the sampling locations of the CTD casts have been recorded using a global positioning system (GPS) navigation device since 1992. Thus, the data for the last 20 years (1995 to 2014) contain most of the oceanic variability via accurate samplings in time and space. These surveys were conducted along the cross-shore lines off the western (YS; Lines 307 to 314), southern (SS; Jeju Island and Korea Strait; Lines 400 and 203 to 207), and eastern (EJS; Lines 102 to 107, 208, and 209) areas of the Korean Peninsula within approximately 200 km of the coast (Fig. 1b). The CTD stations are placed with a spacing of approximately 0.5° and 0.3° in the meridional and zonal directions, respectively, and they are numbered from 0 to 11 for nearshore to offshore regions except for stations on Line 400 (e.g. 12th to 27th stations). Line 400 is included in the SS because the samples on that line well represent the variability across and along the SS and close to Jeju Island. Lines 208 and 209 are grouped into the EJS domain because the data on these two lines have consistent physical properties associated with the NKCC and TWC (Kim and Kim, 1983; Hirose et al., 1996; Yun et al., 2004). The stations with identical cross-shore station numbers are nearly aligned along the same longitude except for certain stations in the YS (e.g. 1st, 2nd, and 3rd stations on Lines 307 to 309) and EJS (e.g. 0th to 5th stations on Lines 102 to

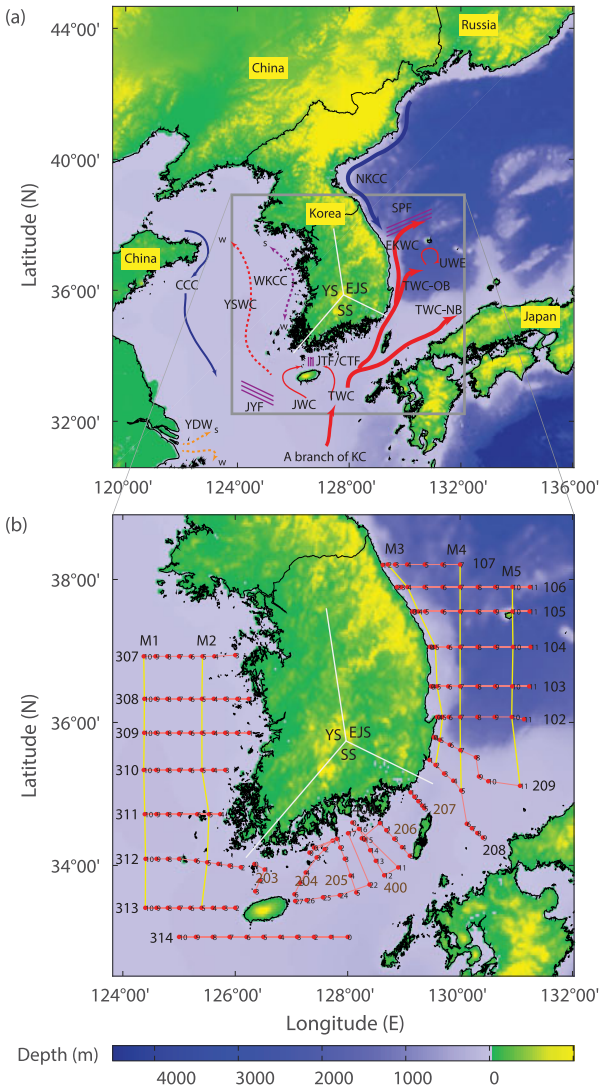

Fig. 1. (a) Schematic regional circulation around the Korean Peninsula. Blue, red, purple, and orange colors indicate the water temperature of cold, warm, fronts, and riverine waters, respectively. Solid and dashed curves denote the persistent and seasonal currents, respectively (s and w indicate the directions of currents in summer and winter, respectively). Acronyms of primary regional currents are listed in the order of the Yellow Sea (YS), South Sea (SS), and East/Japan Sea (EJS): Yellow Sea Warm Current (YSWC), West Korea Coastal Current (WKCC), Chinese Coastal Current (CCC), Jeju Warm Current (JWC), Jeju Tsushima Front (JTF)/Cheju Tsushima Front (CTF), Jeju Yangtze Front (JYF), Yangtze Diluted Water (YDW), Kuroshio Current (KC), North Korea Cold Current (NKCC), Tsushima Warm Current (TWC), Tsushima Warm Current-Nearshore Branch (TWC-NB), Tsushima Warm Current-Offshore Branch (TWC-OB), East Korea Warm Current (EKWC), Subpolar Front (SPF), and Ulleung Warm Eddy (UWE) (see Table 1 for more details). (b) Historical hydrographic survey lines and stations for conductivity-temperature-depth (CTD) profiles for a period of recent 20 years (1995 to 2014) are marked with red lines and black dots, respectively. Three sub-regions are divided into the YS (Lines 307 to 314), SS (Lines 400, and 203 to 207), and EJS (Lines 102 to 107, 208, and 209) regions. CTD stations at each line are numbered with from 0 to 11, corresponding to nearshore to offshore regions except for stations on Line 400 (12th to 27th stations). Five meridional lines ($M1$ to $M5$) are marked with yellow lines.

107). Note that the identification number of the sampling stations ranges from 0 (0th station) to 10 (10th station). Zonal sections on all available sampling lines and meridional sections on five sampling lines (two in the YS and three in the EJS; Fig. 1b) are considered to examine the cross-shore and along-shore structures of the temperature and salinity and the relevant circulations in the meridional and zonal directions, respectively (see Section 2.4.2 for more details).

Table 1. Acronyms and full names of the regional currents and water masses around the Korean Peninsula are listed as a regional order (YS, SS, and EJS) and an alphabetical order.

Acronym	Full name
YSWC	Yellow Sea Warm Current
WKCC	West Korea Coastal Current
CCC	Chinese Coastal Current
YSBCW	Yellow Sea Bottom Cold Water
YSSW	Yellow Sea Surface Water
JWC	Jeju Warm Current
JTF	Jeju Tsushima Front
CTF	Cheju Tsushima Front
JYF	Jeju Yangtze Front
YDW	Yangtze Diluted Water
KC	Kuroshio Current
NKCC	North Korea Cold Current
TWC	Tsushima Warm Current
TWC-NB	Tsushima Warm Current-Nearshore Branch
TWC-OB	Tsushima Warm Current-Offshore Branch
EKWC	East Korea Warm Current
SPF	Subpolar Front
UWE	Ulleung Warm Eddy
ESIW	East Sea Intermediate Water
ESPW	East Sea Proper Water

In this paper, the CTD data for the most recent 20 years (1995 to 2014) are analyzed, and individual CTD profiles are linearly interpolated at the common vertical depths of 0, 5, 15, 25, 35, ..., 175, 185, 200, 220, ..., 480, and 500 m with vertical spacings of 10 and 20 m. The temporal data availability at each line and station is counted when both the temperature and salinity profiles at a given time and station are available more than 50% of the time over all sampling depths (not shown). Although the individual data profiles are obtained from the CTD casts conducted in the research vessels approximately every two months, the full data set may have unevenly spaced time stamps among the stations and lines (see Fig. A1c for examples), and this unevenness may represent a limitation for analysis of the data with composite averages in time because the phases can be smeared. The observational noise and signal-to-noise ratios of the data at the annual and semiannual frequencies adopted in the regression analysis are presented in Appendix A.

2.2. Flagging outliers and the upper limit of the number of realizations

Outliers in the temperature and salinity profiles are flagged when (1) the data have physically inconsistent and inappropriate vertical inversions and (2) the residuals in the applied regression analysis are significant (Section 2.4). The flagged outliers are excluded from the following analysis. For instance, outliers in the salinity profiles are easily identified by large values resulting from a slow response of the conductivity sensor. We conducted a simple QAQC test on the data instead of applying constraints based on specific characteristics of the water properties in the study domain, and this test has been adopted in the QAQC of the Argo CTD profiles (Wong et al., 2003). Flagging with a specific range of values can be misleading and may not be applicable to data with a long-term trend or interannual variability (e.g. linear trend and climate indices-coherent signals). When the number of records at a given location and depth is less than 50% of the expected number of records (i.e. 120 samples obtained from six bimonthly samples per year for the last 20 years), the data are not included in the following analysis because of the insufficient number of observations.

2.3. Representation of the density structure

To identify the regional characteristics of the water masses, joint probability density functions (PDFs) of all available temperature and salinity data at all depths in the entire domain and three regions of the YS, SS, and EJS are overlaid with *T*/*S* diagrams (Fig. 2), which are characterized by the regional circulations, in-and-out flows, and primary driving forces and mechanisms. Density anomalies of the seawater in the EJS are greatly dependent on temperature rather than salinity because the width of variations of the salinity (34 to 34.5) is smaller than that of the temperature (3 to 30°C) (Fig. 2d). Conversely, the density anomalies in the YS vary within a narrow range between 25 and 26 kgm^{-3}, and the ranges of the corresponding temperature and salinity are broader than those in the EJS and SS. Thus, small scale mixing and regional density compensation (e.g. double diffusion) are frequently observed in the YS (Pond and Pickard, 1983) (Fig. 2b). Additionally, the dominant water properties in the SS correspond to the salinities of 33.5 to 34.5 and temperatures of 12 to 18°C, and these properties slightly overlap with the characteristics found in the YS and EJS (Fig. 2c).

2.4. Regression analysis

2.4.1. Temporal mean, annual and semiannual cycles, and residuals. The time series of the temperature (and salinity; $1 \times N$ row vector) at a single location and depth is decomposed into a sum of the temporal mean ($\langle \mathbf{d} \rangle$) and the annual and semiannual components ($\mathbf{d}_S$), polynomial functions (e.g. zeroth and first order polynomials; $\mathbf{d}_F$), and residuals ($\mathbf{d}_R$) (Kim and Cornuelle, 2015):

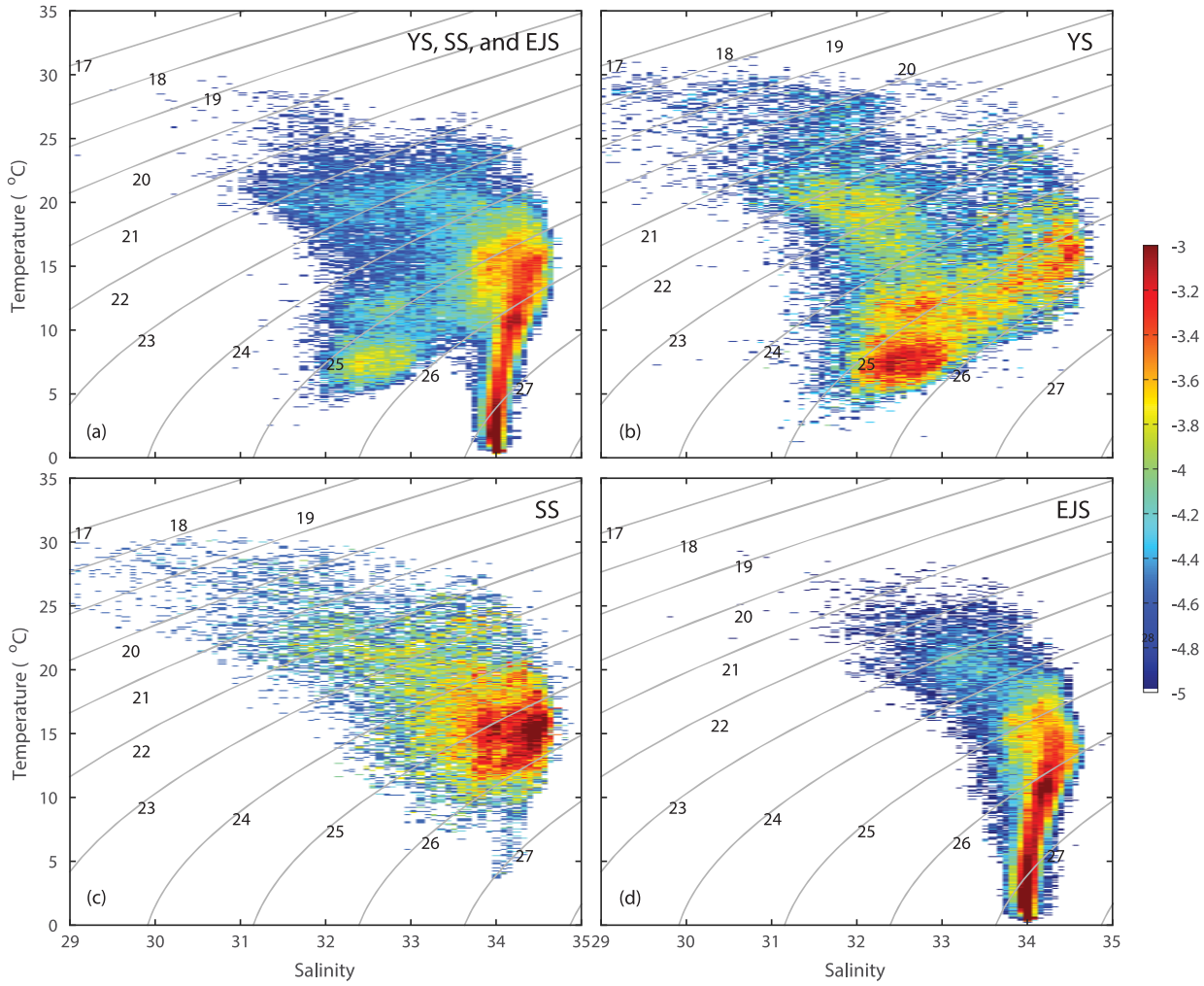

Fig. 2. Joint probability density functions ($\log_{10}$ scale) of the available temperature and salinity data at all depths for a period of recent 20 years (1995 to 2014) in the entire domain and three regions of the YS, SS, and EJS are overlaid with *T*/*S* diagrams. Bin sizes of the temperature and salinity are equal to 0.08°C and 0.08, respectively. Gray contours denote the density anomalies ($\rho' = \rho - 1000, \mathrm{kgm}^{-3}$). (a) Entire domain. (b) YS (Lines 307 to 314). (c) SS (Lines 400 and 203 to 207). (d) EJS (Lines 102 to 107, 208, and 209).

$$\mathbf{d}(t) = \langle \mathbf{d}(t) \rangle + \mathbf{d}_\mathrm{S}(t) + \mathbf{d}_\mathrm{F}(t) + \mathbf{d}_\mathrm{R}(t), \tag{1}$$

$$= \langle \mathbf{d}(t) \rangle + \begin{bmatrix} \mathbf{G}_\mathrm{S} & \mathbf{G}_\mathrm{F} \end{bmatrix} \begin{bmatrix} \mathbf{m}_\mathrm{S} \\ \mathbf{m}_\mathrm{F} \end{bmatrix} + \mathbf{d}_\mathrm{R}(t), \tag{2}$$

$$= \langle \mathbf{d}(t) \rangle + \mathbf{G}\mathbf{m} + \mathbf{d}_\mathrm{R}(t), \tag{3}$$

where a matrix $\mathbf{G}_\mathrm{S}$ ($2K \times N$ dimensions) contains the time series with N records of the sine and cosine functions at the annual and semiannual frequencies (SA_1 and SA_2):

$$\mathbf{G}_\mathrm{S} = \begin{bmatrix} \cos\sigma_1 t_1 & \cdots & \cos\sigma_1 t_N \\ \vdots & \ddots & \vdots \\ \cos\sigma_K t_1 & \cdots & \cos\sigma_K t_N \\ \sin\sigma_1 t_1 & \cdots & \sin\sigma_1 t_N \\ \vdots & \ddots & \vdots \\ \sin\sigma_K t_1 & \cdots & \sin\sigma_K t_N \end{bmatrix}, \tag{4}$$

and $\sigma_k = 2\pi k/365.2425$ [radian per day (rpd)] ($k = 1$ and 2, $K = 2$). The typical sampling time interval is approximately two months and the corresponding Nyquist frequency is approximately three cycles per year, which is higher than semiannual frequencies (see Yoo et al. (2018) and Lee and Kim (2018) for more details). Thus, the proposed regression analysis sufficiently resolves the variance at the annual and semiannual frequencies.

A matrix $\mathbf{G}_\mathrm{F}$ ($2 \times N$ dimensions) represents the time series with two polynomial functions (zeroth and first orders) as the temporal mean and linear trend, respectively,

$$G_{F,1} = \frac{1}{N}, \tag{5}$$

$$G_{F,2} = \frac{2(t-\bar{t})}{\max(t) - \min(t)}, \tag{6}$$

where $\bar{t}$ denotes a center of the time axis. The temporal mean [$\langle \mathbf{d}(t) \rangle$] of the time series at a given location and depth can be biased because of irregular temporal sampling. Thus, the temporal bias is estimated according to the difference between the two temporal averages of the regressed data and sampled data (Kim and Cornuelle, 2015), and then updated to generate an accurate estimate of the temporal mean of the individual time series (see Appendix B for more details of the implemented inverse method).

Monthly composite means and cyclo-stationary empirical orthogonal functions (EOFs) have been used in climatological data analyses of satellite-derived observations (e.g. sea surface temperature and sea surface height anomalies) (Yun et al., 2004; Lim et al., 2012; Kim et al., 1996). However, these methods may not be applicable to time series with uneven time intervals. Using a boxcar average of the time series or a monthly composite mean may smear the phase information and limit the interpretation of the variance at higher frequencies. In addition, the proposed analysis may not be applicable to the time series that contain annual variance modulated by slowly varying signals. Thus, we examine whether the annual variance in the given sample time series is modulated by low-frequency signals in Appendix C to justify the given regression analysis. The significance of individual and total basis functions is determined by the skill, which is the fraction of variance explained by individual or entire basis functions (Appendix D and Equation D1) and estimated amplitudes.

2.4.2. Presentation of the regression analysis. The results of the regression analysis are presented as the zonal and meridional sections of the concatenated vertical profiles. The zonal sections are presented separately for the different maximum depth ranges in the YS, SS, and EJS (Figs. 1b, 3–6, A2, and D1). In each panel within a given hydrographic line, the area from left to right corresponds to nearshore (n) to offshore (o) to the right of Line 312 and offshore (o) to nearshore (n) to the left of Line 312 (e.g. Figs. 3a and 3b). The meridional sections on the five lines are presented ($M1$ and $M2$ in the YS and $M3$, $M4$, and $M5$ in the EJS; Figs. 1b, and 7–9). The gray area indicates the lower bathymetric limit and the white area denotes a vertical separator of the individual hydrographic lines or the regions where the data are excluded because of outliers or an insufficient number of observations. In addition, the layered-color scheme was chosen to present the regression outcomes, which allows us (1) to identify the layered and noisy structures and small range variation more easily than the monotonically increasing or decreasing or two-ends color schemes do and (2) to avoid an extra interpolation to draw contours or isovalue lines (Figs. 3–5, 7, and 8). In the presentation of the annual and semi-annual phases, the phase is converted into the month of the year, which helps us to recognize when the given variable reaches the maximum in the annual and semi-annual frameworks intuitively.

3. Results

3.1. Temporal mean and standard deviation

The temporal mean of the temperature is highest in the SS and decreases toward the YS and EJS, and the warm temperature is closely related to the intrusion of the TWC (Kang and Jin, 1984b; Chang et al., 2004; Park and Chu, 2006) (Figs. 3a–3c). The two-layered temperature profiles in the YS, the gradual vertical gradients in the SS, and the offshore downward tilts of the isothermal lines in the EJS characterize the regional circulation and stratification, and are associated with surface and subsurface mixing and heat penetration (Figs. 3a–3c). The higher standard deviations of the temperatures in the upper 25 m depth of the YS are related to annual surface heating and cooling, and the enhanced standard deviations of subsurface temperatures in the EJS can be linked to interannual variability in regional mesoscale eddies and boundary currents (Chang et al., 2004; Kim and Min, 2008; Lee and Kim, 2018) (Figs. 3d–3f).

The temporal mean of the salinity shows an increase from the YS to the SS and the EJS with depth, except for the maxima observed at the TWC boundary in the EJS between depths of 50 m and 150 m (Chang et al., 2004) (Figs. 3g–3i). Both the horizontal and vertical gradients of the temporal mean of the salinity appear significant in the YS and SS because of the confluence of the saltier Kuroshio Current (KC) or its branch flow in the SS and the fresher water driven by dominant tidal mixing in the YS. For example, horizontal and vertical salinity gradients are observed on Lines 313, 314, 203, and 204 because of (1) fresh water in the upper water column and nearshore and (2) salty water in the lower water column and offshore. Similarly, the standard deviations of the salinity become significant in the upper 50 m of the water column in the SS because of intermittent freshwater inputs from the Yangtze River and the persistent intrusion of the KC (Lines 313, 314, 400, 205, 206, and 207) (Figs. 3j–3l).

3.1.1. Yellow Sea and South Sea. The isothermal lines and isohalines on Lines 313 and 314 in the YS and Lines 203 to 206 in the SS are sloped out of phase in the cross-

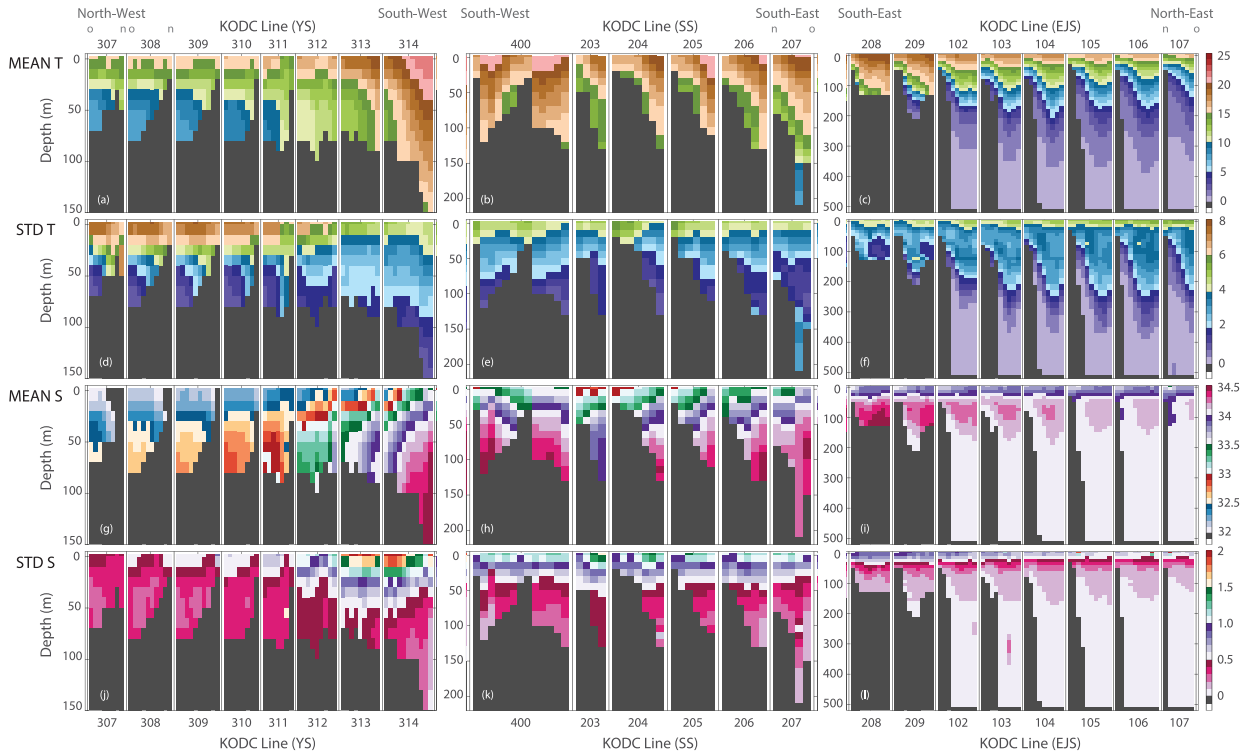

Fig. 3. Zonal sections of the temporal mean ($\langle \mathbf{d} \rangle$) and standard deviation ($\langle \mathbf{d}^2 \rangle^{1/2}$) of the temperature (°C) and salinity profiles sampled in the YS, SS, and EJS for a period of recent 20 years (1995 to 2014). (a–c) Temporal mean of the temperature. (d–f) Standard deviation of the temperature. (g–i) Temporal mean of the salinity. (j–l) Standard deviation of the salinity. (a), (d), (g), and (j): YS. (b), (e), (h), and (k): SS. (c), (f), (i), and (l): EJS. The vertical profiles are concatenated in terms of cross-shore lines, and the unsampled depths and bottom bathymetry are shown as gray columns.

shore direction, i.e. upward tilting isothermal lines and downward tilting isohalines onshore. A similar case, which appears as northward tilting isothermal lines and southward tilting isohalines, is found on Lines 312 and 314 in the YS (Park and Chu, 2006) (Figs. 3a, 3b, 3g, 3h, 7a, 7g, 8a, and 8g).

Two different water properties are observed in the YS and SS: (1) cold and less saline water represents the tidally mixed coastal waters, and (2) warm and saltier water indicates the influence of the TWC branches, which include persistent fronts throughout the year in the SS (Na et al. (1990); Jeju Tsushima Front (JTF) in Park and Chu (2006), also called the Cheju Tsushima Front) and are partially dominant during winter in the YS (e.g. Jeju Yangtze Front (JYF) in Park and Chu (2006)) (Figs. 3a, 3b, 3g, and 3h). In these regions, double diffusion tends to appear as a result of colliding water masses that have a similar order of density (Pond and Pickard, 1983; Son et al., 2010) (Fig. 2b). The vertical stratification in the YS appears relatively well mixed in winter and stratified in summer. Thus, the temporal mean of the temperatures on Lines 307 to 312 becomes cooler in the upper layer and warmer in the lower layer shoreward, and this effect can be associated with the dominant tidal mixing in summer (Lie, 1989; Jeong et al., 2009).

Cold water appears near the coast of the SS because of tidal mixing and persistent intrusions of the Jeju Warm Current (JWC) and TWC on the western and eastern sides of Jeju Island. These water masses generate the JTF throughout the year (Park and Chu, 2006; Pang et al., 2003). The north-south tilts of the isothermal lines in this region generate the eastward relative geostrophic currents, which have been consistently observed within in-situ current profilers (Pang et al., 2003) (Figs. 7a and 7g). The oppositely tilted temperature and salinity along the JYF yield the density compensation (Park and Chu, 2006) (Figs. 3a and 3g).

Less saline water appears in the northern area of the YS (Lines 307 to 311) partially because of fresh waters from local rivers (e.g. Han River, Kum River, and Amnok River) (Hwang et al., 2014) (Fig. 3h). Similarly, the higher standard deviations of the salinity in the SS can be explained by the influence of freshwater from the Yangtze River (Fig. 3k).

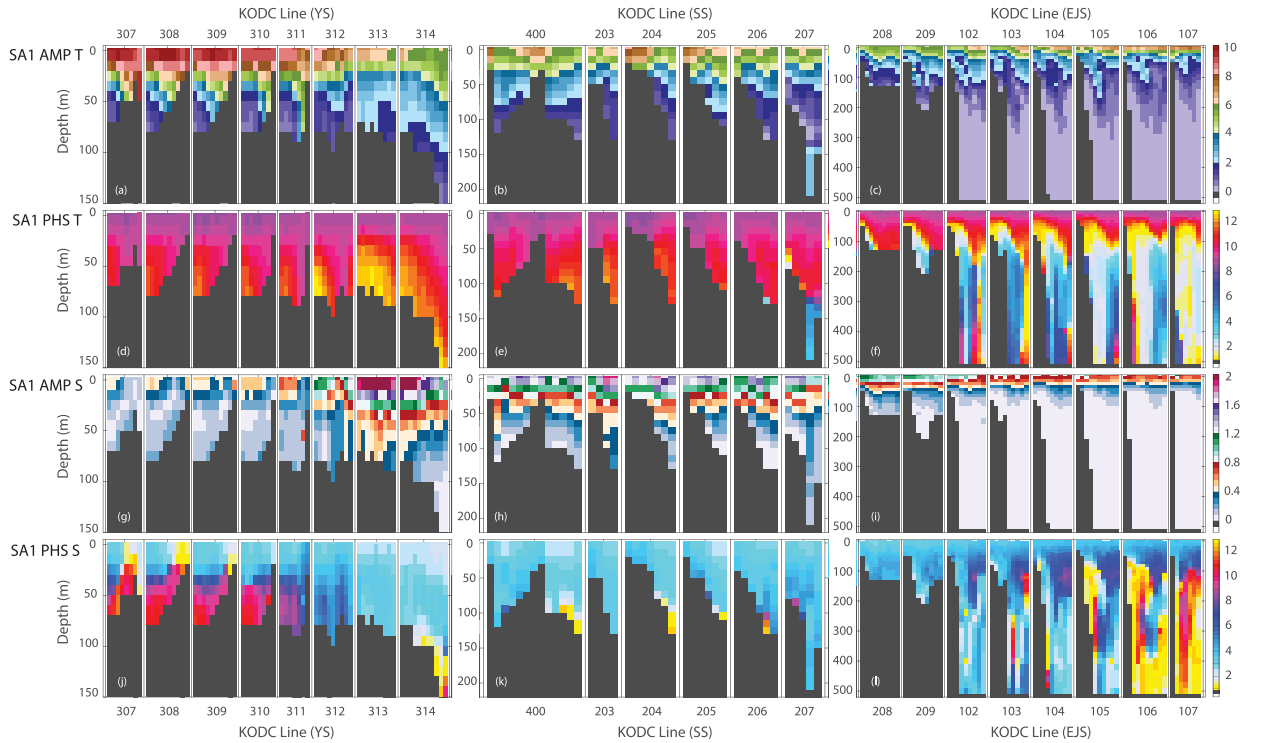

Fig. 4. Zonal sections of the annual amplitudes and phases (SA_1) of the temperature (°C) and salinity profiles sampled in the YS, SS, and EJS for a period of recent 20 years (1995 to 2014). (a–c) Annual amplitudes of the temperature. (d–f) Annual phases of the temperature. (g–i) Annual amplitudes of the salinity. (j–l) Annual phases of the salinity. (a), (d), (g), and (j): YS. (b), (e), (h), and (k): SS. (c), (f), (i), and (l): EJS. The vertical profiles are concatenated in terms of cross-shore lines, and the unsampled depths and bottom bathymetry are shown as gray columns. The phase is converted into the month of the year.

3.1.2. East/Japan Sea. The temporal mean of the temperature in the EJS is tilted downward onshore in the upper 500 m and southward in the upper 300 m, and these findings are associated with the northeastward relative geostrophic currents (Fig. 3c). As the regional southward current, the NKCC has been persistently found at depths of 100 to 400 m (within 50 km of the shoreline) in the region (Kim and Kim, 1983; Kim et al., 2009). The geostrophic currents estimated from observations have been reported as the currents referenced below at least 500 m [e.g. referenced at 1280 m in Chang et al. (2002a), 700 m in Shin et al. (1995), and 500 m in (Yun et al., 2004) and at an isopycnal depth of the interface of the NKCC and TWC in Byun and Chang (1984)]. Intermittent onshore tilts of the isothermal lines below 200 m are observed in the time series of temperature profiles, and these tilts enhance the southward subsurface currents near the coast.

In addition, three vertically layered distinct water properties are observed in the meridional sections of the temporal means of the temperature and salinity (Figs. 3c, 3f, 7m, 7s, and 7y in the upper 500 m and Figs. 8m, 8s, and 8y in the upper 100 m). These properties have been identified with water masses of the TWC, ESIW, and East Sea Proper Water (ESPW) (Chang et al., 2015). However, a salinity minimum is not observed in the middle layer, and this finding is inconsistent with the historical ESIW properties (Kim and Kim, 1999; Chang et al., 2002a) because (1) the temporal mean is subjective to the length of the time window and (2) the salinity minimum may not be the persistent features. The thickness of the middle layer decreases toward the south, i.e. the upper and lower interfaces deepen southward and northward, respectively (Talley et al., 2006), and this effect generates relative eastward and westward geostrophic currents, respectively, and baroclinic instability [e.g. the Subtropical Countercurrent (STCC) and North Equatorial Current (NEC) system between 15°N and 30°N observed in the North Pacific in Qiu et al. (2014)].

The UWE is located approximately 120 to 170 km from the coast on Lines 102 to 106 in Fig. 1a, which is partially consistent with Chang et al. (2004) and Cho et al. (1990). The temporal mean of the temperature may smear the vertical structures of the UWE (e.g. slopes and

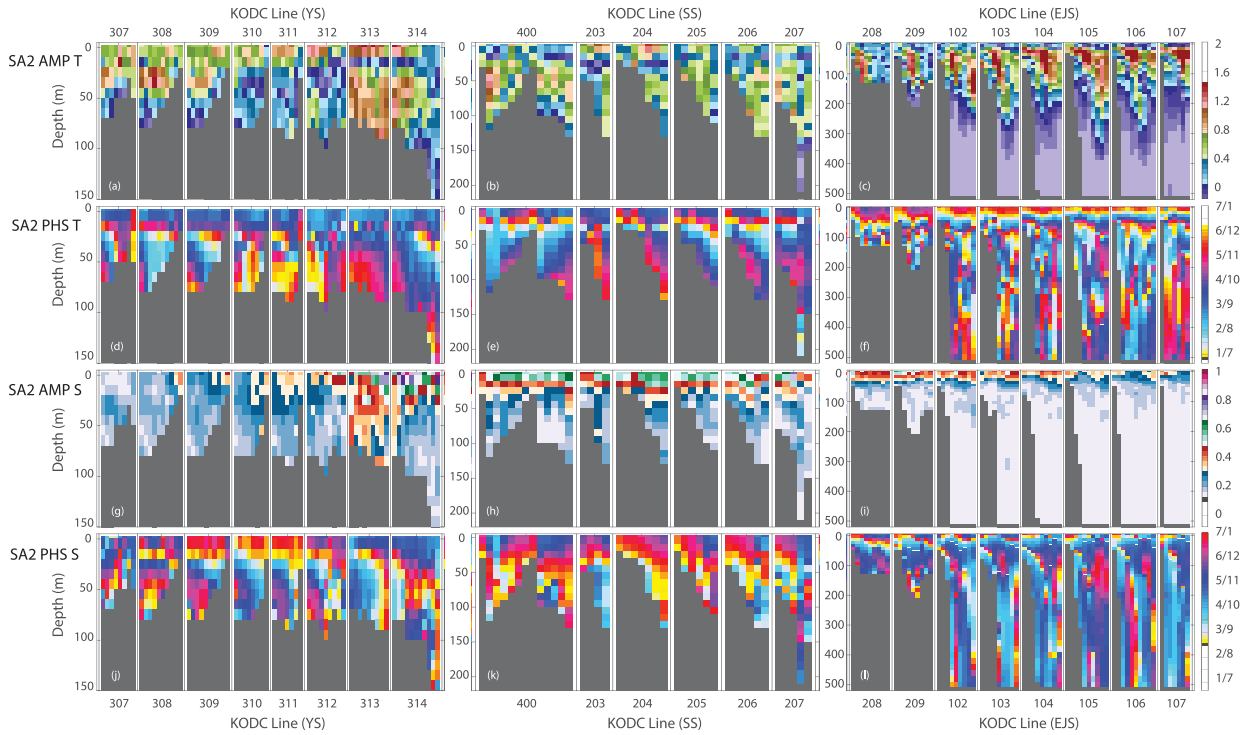

Fig. 5. Zonal sections of the semi-annual amplitudes and phases (SA_2) of the temperature (°C) and salinity profiles sampled in the YS, SS, and EJS for a period of recent 20 years (1995 to 2014). (a–c) Semi-annual amplitudes of the temperature. (d–f) Semi-annual phases of the temperature. (g–i) Semi-annual amplitudes of the salinity. (j–l) Semi-annual phases of the salinity. (a), (d), (g), and (j): YS. (b), (e), (h), and (k): SS. (c), (f), (i), and (l): EJS. The vertical profiles are concatenated in terms of cross-shore lines, and the unsampled depths and bottom bathymetry are shown as gray columns. The phase is converted into the month of the year.

boundaries of isothermal lines) because of interannual characteristics. To the east of the UWE, the upward tilts of isothermal lines are clearly visible, which implies southward relative geostrophic currents as one of paths of the NKCC (Line 102 to 107 in Figs. 3c and 3f) (Kim and Kim, 1999; Chang et al., 2002a). Although the southward path of the NKCC is known to be close to the east coast of Korea, recent studies have reported multiple southward paths (Kim and Min, 2008).

The standard deviations of the temperatures in the lower layer (Fig. 3f) are likely enhanced because of changes in the width of the UWE (Chang et al., 2002b; Shin et al., 2005). The reduced standard deviations in the upper layer appear as bright turquoise above (as opposed to the normal or enhanced standard deviations as dark turquoise below) Lines 102, 103, and 104 in Fig. 3f, and are associated with the eddy thermostad layer, which maintains a temperature of approximately 10°C (Hogan and Hurlburt, 2006).

The local maxima of the temporal mean of the salinity are found between 50 m and 150 m (Figs. 3i, 8m, 8s, and 8y) as part of the boundary of the TWC (Chang et al., 2004) (Fig. 3i). The zonal width of the saline water becomes narrower to the south because of zonal shrinking of the cold water (NKCC) during its intrusion into the warm water (TWC) (Lie and Byun, 1985; Jeong et al., 2013).

3.2. Annual and semiannual variability

The annual amplitudes of the temperatures in the surface layer (upper 50 m) are dominant and have regional variations of 8 to 10°C (YS), 6 to 8°C (EJS), and 4 to 6°C (SS) (Figs. 4a–4c). The vertical penetration of the annual variability is slightly stronger in the YS (up to 50 m) than in the EJS and SS (up to 30 m). The vertical stratification becomes significant due to solar radiation in summer, and the water columns become well-mixed due to wind stress and surface cooling in winter (Kang and Jin, 1984b; Hwang et al., 2014). The annual phases of the temperature increase vertically, indicating the timing of the maximum temperature. For example, the temperature reaches a maximum in mid-August (upper 50 m), November (100 to 200 m), and March of the following year (400 to 500 m) in the EJS. Moreover, the annual

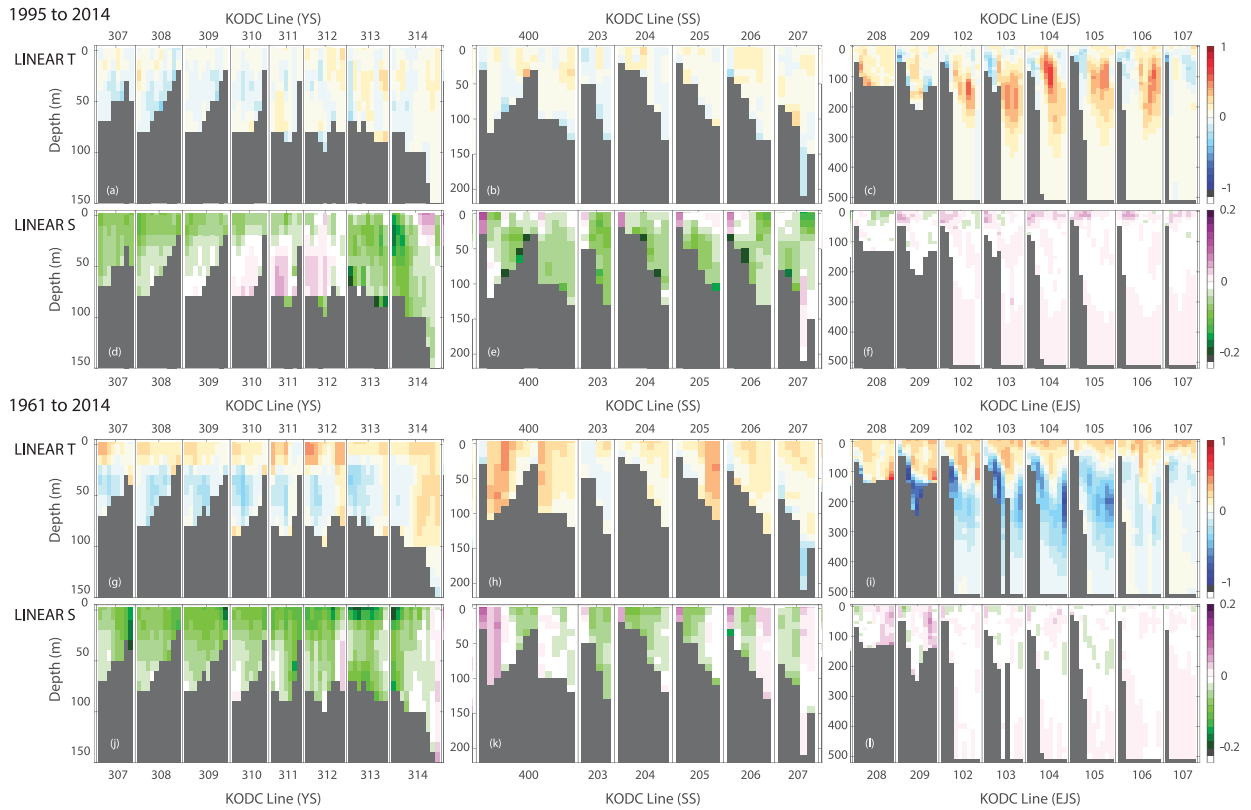

Fig. 6. Zonal sections of the linear trend of the temperature (°C) and salinity profiles sampled in the YS, SS, and EJS for a period of recent (a–f) 20 years (1995 to 2014) and (g–l) 54 years (1961 to 2014). The linear trend is presented as the value for 10 years. (a–c) Linear trend of the temperature. (d–f) Linear trend of the salinity. (g–i) Linear trend of the temperature. (j–l) Linear trend of the salinity. The vertical profiles are concatenated in terms of cross-shore lines, and the unsampled depths and bottom bathymetry are shown as gray columns.

phases penetrate more slowly offshore than onshore in the EJS, and the isophase lines in September (magenta) appear at 35 m onshore and 55 m offshore.

The annual amplitudes of the salinity have maxima on Lines 313 and 314, where the seasonal influence of the freshwater flowing from the Yangtze River is dominant (Fig. 4g). The annual phases of the salinity indicate that the water in the upper layer (0 to 50 m in the YS and SS; 0 to 100 m in the EJS) is mostly fresh in early (YS and SS) and late (EJS) September and salty in early (YS and SS) and late (EJS) March (Figs. 4j–4l).

3.2.1. Yellow Sea and South Sea. The annual amplitudes of the temperatures in the YS (Lines 307 to 312) exhibit a two-layer structure of more than 9°C above 25 m and less than 4°C below 25 m (Fig. 4a), and this structure can be explained by the (1) trapping of the surface heat fluxes above the thermocline in summer and (2) surface mixing and cooling because of the surface wind in winter (Park and Chu, 2006; Zhang et al., 2008). The annual amplitudes are tilted southward (Fig. 7b), and the annual phases (Fig. 7d) have a maximum in November below 50 m depth that can be explained by the annual YSBCW (Park and Chu, 2006), which is formed under a strong thermocline in summer and retains cold water (less than 10°C) at a depth of 50 to 75 m in the region of 34°N to 37°N and 121°E to 126°E (Zhang et al., 2008; Hu et al., 1991). The trapped cold waters flowing from the north (Wang et al., 2014; Zhang et al., 2008) and tidal residual currents may induce the YSBCW and intermittently appear in the northern SS during summer (Pang et al., 2003; Moon et al., 2009). Alternatively, the YSWC is found to intrude northwestward during winter and prevent the southward residual currents. The annual phases of the temperature change gradually in the vertical direction along with the vertical diffusion of surface heat fluxes (Fig. 4d).

The annual amplitudes of the temperature in the cross-shore direction decrease onshore, which is consistent with the influence of the annually modulated tidal mixing

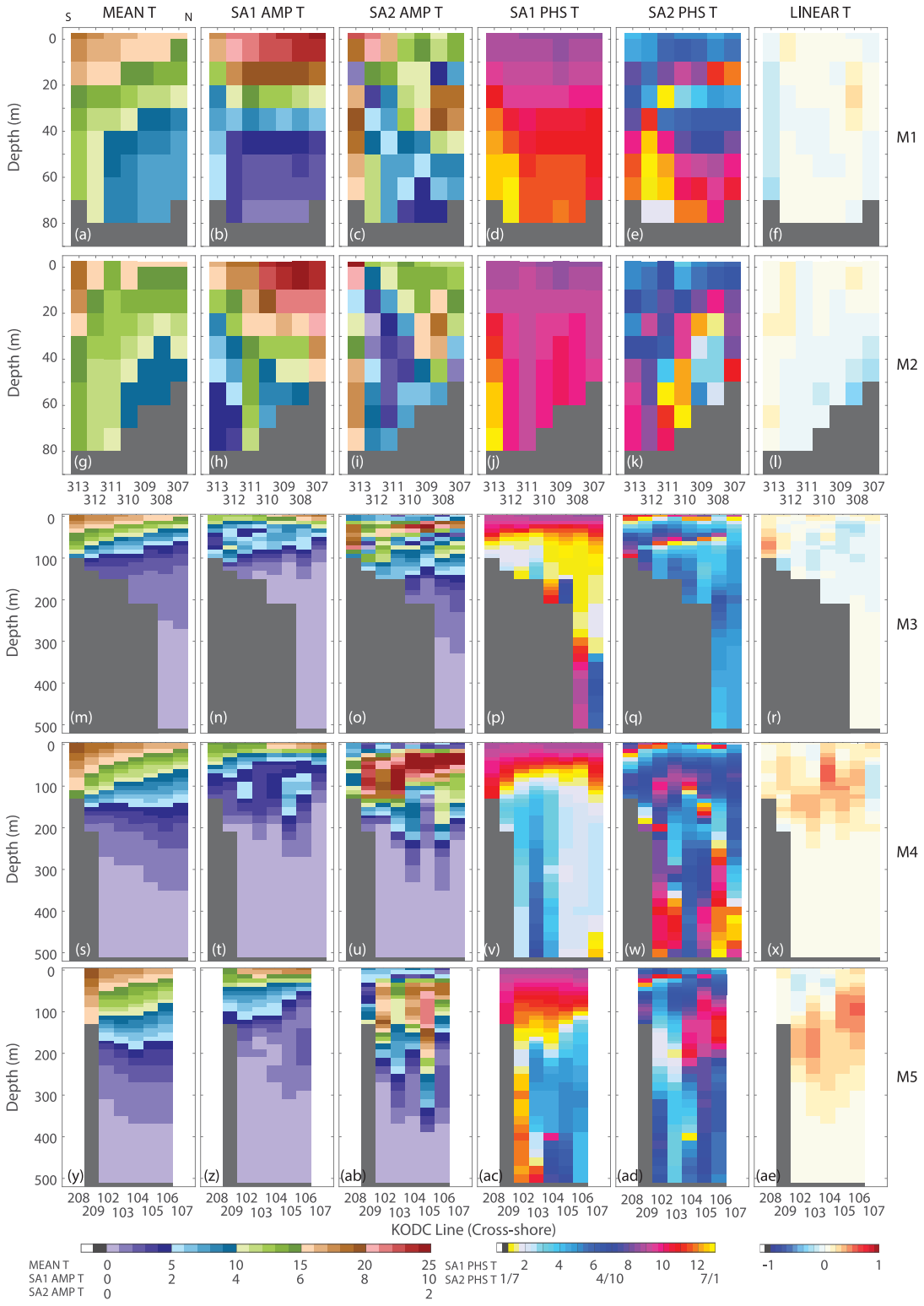

Fig. 7. Meridional sections of the temporal mean, amplitudes and phases at the annual and semi-annual frequencies, and linear trend of the temperature in the YS ($M1$ and $M2$) and EJS ($M3, M4$, and $M5$). (a), (g), (m), (s), and (y): Temporal mean of the temperature. (b), (h), (n), (t), and (z): Annual amplitudes of the temperature (SA_1). (c), (i), (o), (u), and (ab): Annual phases of the temperature (SA_1). (d), (j), (p), (v), and (ac): Semi-annual amplitudes of the temperature (SA_2). (e), (k), (q), (w), and (ad): Semi-annual phases of the temperature (SA_2). (f), (l), (r), (x), and (ae): Linear trend of the temperature. (a–f) $M1$. (g–l) $M2$. (m–r) $M3$. (s–x) $M4$. (y–ae) $M5$. The linear trend of the temperature is presented as the value for 10 years. The vertical profiles are concatenated in terms of cross-shore lines, and the unsampled depths and bottom bathymetry are shown as gray columns. The phase is converted into the month of the year.

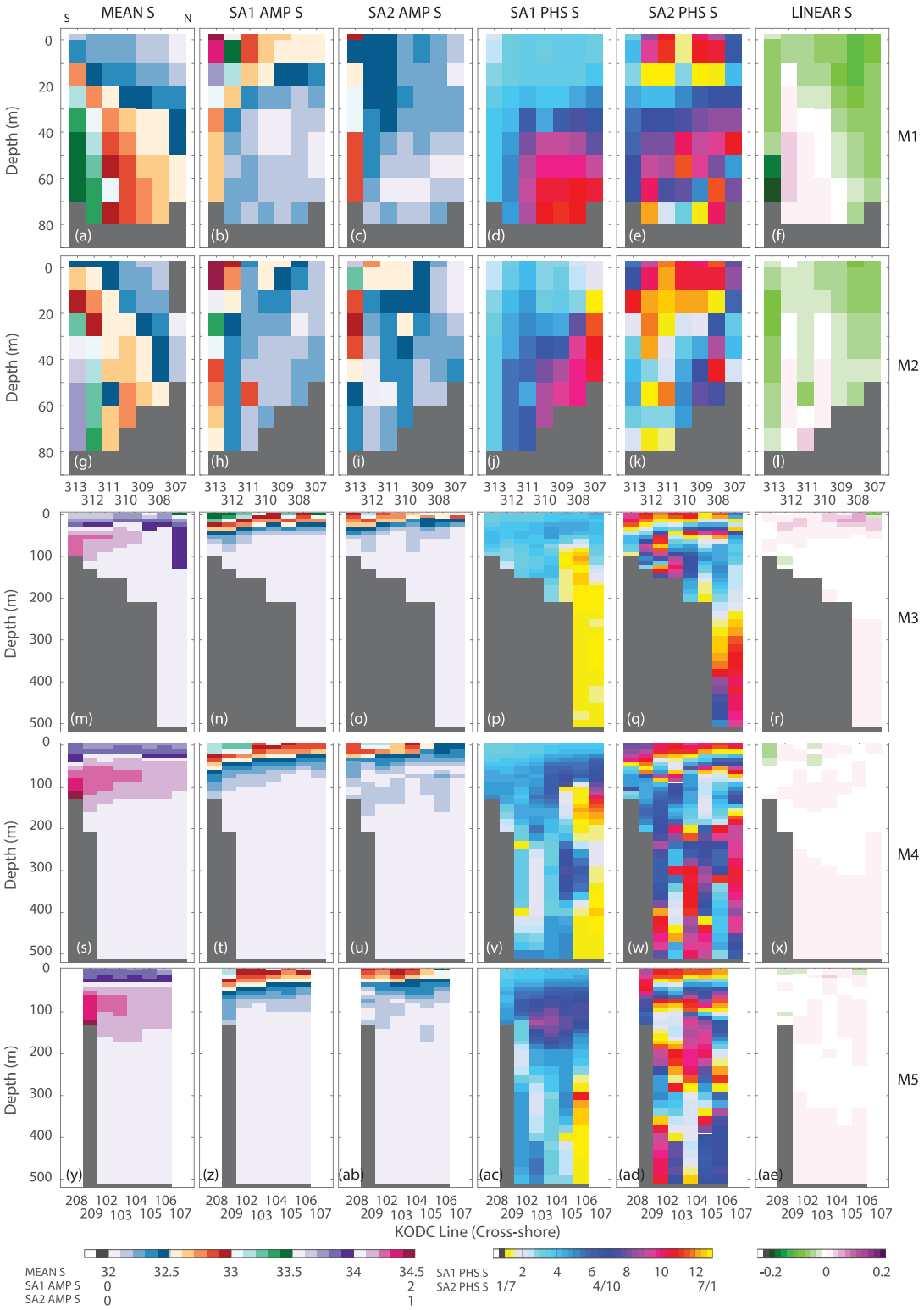

Fig. 8. Meridional sections of the temporal mean, amplitudes and phases at the annual and semi-annual frequencies, and linear trend of the salinity in the YS ($M1$ and $M2$) and EJS ($M3$, $M4$, and $M5$). (a), (g), (m), (s), and (y): Temporal mean of the salinity. (b), (h), (n), (t), and (z): Annual amplitudes of the salinity (SA_1). (c), (i), (o), (u), and (ab): Annual phases of the salinity (SA_1). (d), (j), (p), (v), and (ac): Semi-annual amplitudes of the salinity (SA_2). (e), (k), (q), (w), and (ad): Semi-annual phases of the salinity (SA_2). (f), (l), (r), (x), and (ae): Linear trend of the salinity. (a–f) $M1$. (g–l) $M2$. (m–r) $M3$. (s–x) $M4$. (y–ae) $M5$. The linear trend of the salinity is presented as the value for 10 years. The vertical profiles are concatenated in terms of cross-shore lines, and the unsampled depths and bottom bathymetry are shown as gray columns. The phase is converted into the month of the year.

because the tidal mixing near the coast may break the stratification and generate a vertical temperature gradient. Therefore, the water near the coast becomes cooler in the upper layer and warmer in the lower layer, and this effect results in reduced annual amplitudes compared with those of the offshore temperature (Jeong et al., 2009).

The annual phases of the temperature below 50 m and near the coast (within 20 km of the coast) can be associated with the two annual out-of-phase boundary currents of the WKCC and YSWC (Figs. 1a and 4j).

3.2.2. East/Japan Sea. The gradients of the annual amplitudes of the temperature in the surface layer (less than 50 m depth) in the cross-shore direction decrease offshore (1 to 2°C), and this finding can be interpreted as a footprint of the influence of the onshore coastal currents of the NKCC with weak annual variance and the offshore TWC with dominant annual variance. The iso-annual-amplitude lines of 2°C show that subsurface paths of the TWC become shallower from 100 to 50 m along the southern (Line 102) and northern (Line 106) boundaries of the domain (Kim and Kim, 1983). The annual amplitudes and total standard deviations within 30 km of the coast are weak because of the persistent ESIW in that area (Yun et al., 2004; Chang et al., 2002a). On Lines 208, 209, and 102 to 107, the minimum annual amplitudes and the abrupt annual phase changes appear as a downward tilt between depths of 45 and 185 m.

The annual phases of the salinity exhibit maxima between 50 and 150 m in May in the south and June in the north, and these findings can be interpreted as the (1) northward advection of the saline TWC, (2) vertical diffusion of surface saline water over time, and (3) temporal variation in the core of the NKCC (Fig. 4l).

The semiannual amplitudes of the temperature become significant in the subsurface (50 to 200 m) (Fig. 5c) and are tilted southward (Figs. 8u and 8ab), which is consistent with observations of southward paths of the NKCC based on the semiannual variability in the temperature in this region and the Korea Strait (Min et al., 2006; Kim and Min, 2008). However, the southward-tilted subsurface amplitudes and phases in the meridional sections on Lines 102 to 107 (Figs. 7u and 7w) can be associated with subduction in the subpolar region (Hogan and Hurlburt, 2006; Lee et al., 2006; Yoshikawa et al., 2012), which is aligned with the semiannual amplitudes of the

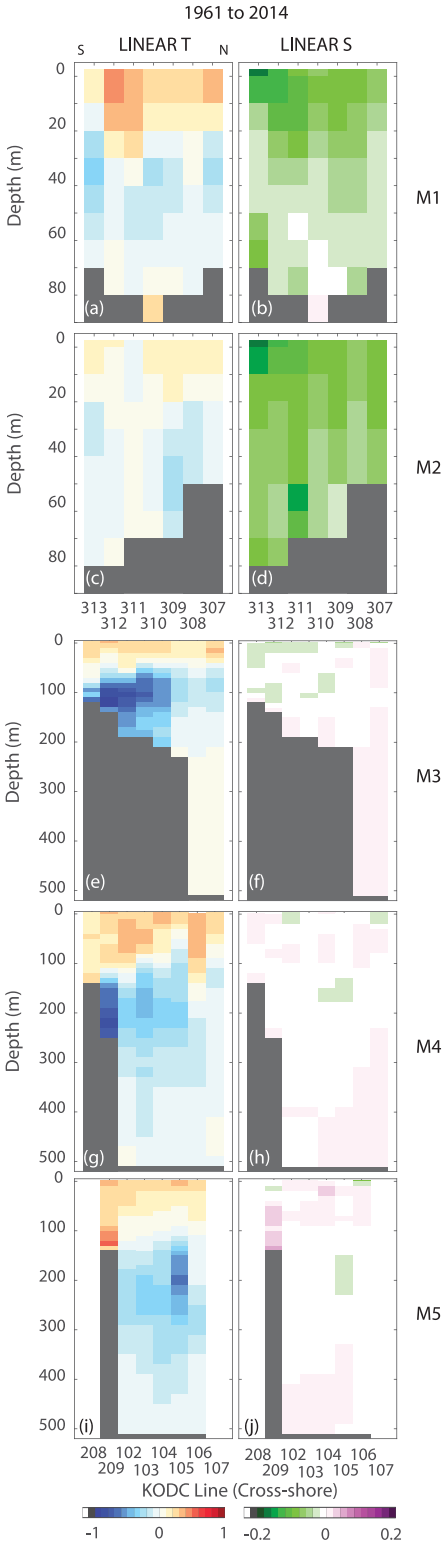

Fig. 9. Meridional sections of the linear trend of the temperature and salinity in the YS ($M1$ and $M2$) and EJS ($M3$, $M4$, and $M5$) for a period of 54 years (1961 to 2014). (a), (c), (e), (g), and (i): Linear trend of the temperature. (b), (d), (f), (h), and (j): Linear trend of the salinity. (a) and (b): $M1$. (c) and (d): $M2$. (e) and (f): $M3$. (g) and (h): $M4$. (i) and (j): $M5$. The linear trend of the salinity is presented as the value for 10 years. The vertical profiles are concatenated in terms of cross-shore lines, and the unsampled depths and bottom bathymetry are shown as gray columns.

dissolved oxygen of approximately 0.25 mlL^{-1} on Lines 208, 209, and 102 to 107 (not shown).

In addition, the semiannual amplitudes of the salinity become dominant in the upper layer (0 to 50 m) and deeper to the south (Figs. 5i, 8n, 8o, 8t, 8u, 8z, and 8ab).

3.3. Linear trend

The linear trends in the temperature in the cross-shore direction in the EJS are negative in the onshore region and surface layer (less than 50 km from the coast and upper 50 to 100 m) and positive in the offshore region and subsurface depth (beyond 50 km and below 50 m) (Figs. 6c, 7r, 7x, and 7ae).

The linear trend estimates can be sensitive to the length of the time records. An identical regression analysis is conducted on all available records of the NIFS CTD data for 54 years (1961 to 2014) by including non-CTD and non-GPS-based observations (Figs. 6g–6l and 9). The estimated linear trends over a longer time window are mostly consistent with the ones over the past 20 years except for the cases with opposite signs, which are the temperature in the EJS and the salinity in the YS (last columns in Figs. 7 and 8; Figs. 6g–6l). In addition, the linear trends based on all available time records exhibit results consistent with those of Yoon et al. (2016) and show a positive (warming) trend in the upper 50 m and a negative (cooling) trend below 50 m based on analysis of the same type as the NIFS CTD data for a period of 32 years (1976 to 2007) in the Ulleung Basin region in Yoon et al. (2016).

One potential mechanism underlying the long-term trend in the EJS is the increased surface heat fluxes in the EJS, and this mechanism occurs prior to the increased vertical heat convection and the southward and downward transport of the heat in the middle layer following the migration of the ESIW. This heat transport appears as a warming tendency in the surface layer and southward and downward traces of warming tendencies in the middle layer (Figs. 6c, 7x, and 7ae).

The linear trends in the salinity are negative in the YS and weakly positive in the EJS and their mixture in the SS (Figs. 6d–6f). The linear trend of the salinity around the Korean Peninsula can be explained by (1) the long-term variability in the salinity caused by intrusion and transport by the regional boundary currents and (2) local evaporation and precipitation (EP) associated with heat fluxes and weather conditions. The linear trend in the water in the YS becomes negative (fresh) and positive (salty) in the northern upper layer and southern lower layer, respectively (Figs. 6d, 8f, and 8l), and this trend can be explained by the relative decrease in the EP in the upper layer and the YSBCW in the lower layer (Zhang et al., 2008; Hu et al., 1991). In the EJS, a long-term trend of increasing salinity is observed because of the influence of the KC or TWC, which flow from the south or southwest and have more saline properties (Figs. 6e, 8r, 8x, and 8ae). In the SS, the water becomes fresher in the offshore upper layer and near-coast lower layer and salty in the near-coast upper layer as part of the two salinity tendencies observed in the YS and EJS (Fig. 6e).

4. Discussion

4.1. Potential drivers of the annual and semiannual variability

The annual temperature at the surface is highly related to the variability in the Siberian atmospheric pressure, which causes decreasing amplitudes and increasing phases to the southeast of the EJS and YS. In the EJS, the interface between onshore and offshore areas has a small annual amplitude (less than 1°C), and the enhanced semiannual variability in the temperature, salinity, and dissolved oxygen is observed near the interface and may be related to the southward advection of the NKCC or subducted water in the subpolar region (frontal area near 38.5°N and 39°N and convection area near northwest in the EJS). In the YS, the semiannual variability in the temperature is highly related to the southward extension of the YSBCW in summer. The annual phases of the temperature and salinity in the southern EJS (Lines 102 to 104) propagate with similar magnitudes and directions to those of the NKCC (onshore) and TWC (offshore), indicating that the advection in these areas is significantly related to heat transfer.

4.2. Residual circulation: Inter-annual variability

The residual components of the proposed analysis in this paper may contain nonseasonal variability, i.e. interannual variability. Prominent regional interannual variability can be found with the UWE (Mitchell et al., 2005; Kim et al., 2002) and ESIW in the EJS.

A clockwise meandering eddy, the UWE, is frequently observed between 37°N and 38°N in the east of the area where the East Korea Warm Current (EKWC) and the NKCC collide, and 20 to 50 km south of Ulleung Island (Cho et al., 1990; Morimoto et al., 2000). The UWE is represented by an isothermal line of 10°C (Lines 103 to 106 in Fig. 3c). The core of the UWE is located at depths between 100 m and 300 m, and its size is primarily influenced by either the magnitude of the EKWC (Chang et al., 2004; Shin et al., 1995; Cho et al., 1990) or the volume transport through the Tsushima Strait (Mitchell et al., 2005). In addition, the ESIW is characterized by

salinities of less than 34.06, potential temperatures of 1 to 5°C, and potential densities of 26.9 to 27.3 kgm^{-3} (Kim and Kim, 1999; Chang et al., 2002a). The southward subducted ESIW (Kim and Chung, 1984; Yoshikawa et al., 1999) and southward coastal subsurface currents (NKCC) have similar water properties except for the relatively low and high dissolved oxygen concentrations, respectively, which are used to distinguish the relative age of the water. The subduction paths of the offshore ESIW have been identified to the left and right of Ulleung Island (Chang et al., 2002a; Yun et al., 2004; Kim and Min, 2008). Other than subduction, the positive wind stress curl or surface cooling due to Siberian cold air may cause surface water to sink (Yun et al., 2004), indicating the origin of the low-salinity water observed near the coast of the EJS and the Ulleung Basin (Yoon et al., 2005). Near the subpolar front, subduction may also appear due to the down-front wind and surface cooling (Lee et al., 2006; Yoshikawa et al., 1999). The substantial standard deviation of the residual temperature between 50 m and 250 m serves as a footprint of the UWE and ESIW (Fig. D1f).

4.3. Relevance with regional climate indices

We hypothesize that the variability in the temperature and salinity around the Korean Peninsula may be related to variance at the annual and its superharmonic frequencies, and the linear trend as well as to the regional interannual climate variability. Thus, we derived the regional climate indices using an EOF analysis of the long-term Siberian high pressure data and sea surface temperature records at the branch of the KC to effectively describe the oceanic variability and conducted a multivariate regression using those basis functions. However, the contributions of these regional climate indices are not sufficient (less than 5% of the total variance) to explain the variability in the temperature and salinity at the surface and in the interior. Thus, the climate indices derived from subsurface temperature and salinity may represent the regional interannual variability. Not only the regional long-term variability and annual variability but also the global-scale climate variability can be better understood with subsurface climate indices rather than surface climate indices (e.g. El Nino Southern Oscillation and Pacific Decadal Oscillation).

4.4. Applications of the derived climatology

The derived climatology of the temperature and salinity profiles obtained from multidecadal hydrographic surveys can be used (1) to elucidate the mesoscale circulation and long-term variability, (2) to provide data-derived boundary conditions of the regional circulation modeling, (3) to design optimal sampling of the mesoscale and submesoscale circulation studies (Yoo et al., 2018; Lee and Kim, 2018), and (4) to evaluate the regional heat and salty budget balances (Yoon et al., 2016). In particular, the observations along and across the submesoscale fronts and eddies using the Lagrangian platform and their optimal sampling designs can benefit, as the derived climatology can be used to identify the edge of the mesoscale eddies and baroclinic instability-favorable regions. Moreover, a similar regression analysis on profiles of oxygen and nutrients (e.g. nitrate, phosphate, and silicate) along with CTD data allow us to investigate the mesoscale physio-biological interactions (e.g. regional chlorophyl blooms) (Lee and Kim, 2018).

5. Summary

We derived the coastal ocean climatology of the temperature and salinity around the Korean Peninsula obtained from long-term hydrographic surveys conducted over the last 20 years (1995 to 2014) by performing a multivariate regression analysis using basis functions of the temporal mean, annual and semiannual cycles, and linear trend. We reviewed the regional mesoscale circulation with regard to the boundary currents, geostrophic currents, and density compensation and layered density structures associated with distinct water properties based on the individual components of the regression in the zonal and meridional directions. In the temporal means, the onshore southward NKCC and the offshore northeastward TWC, a three-layered meridional structure of the TWC, ESIW, and ESPW results in zonal geostrophic currents in the EJS. The oppositely sloping isothermal lines and isohalines in the cross-shore (SS) and meridional (YS) directions are associated with regional density compensation and weak baroclinic relative geostrophic currents in the YS and SS. The annual and semiannual variability in the temperature in the EJS primarily appears in the surface (upper 50 m) and intermediate (between 50 m and 200 m) layers, respectively, because of annual surface heat fluxes and southward subsurface regional currents. For the linear trend in the temperature, the onshore decreasing and offshore increasing tendencies in the EJS are described by the transport of long-term heat contents associated with the regional boundary currents. The proposed multivariate regression analysis explains approximately 90% of the variance in the temperature and salinity in the upper 100 m (corresponding to most of the depths in the YS and SS) and has limitations in capturing the subsurface variability. In the context of the local-, regional-, and global-scale circulations, the given analysis and derived climatology can be used as a resource for the observation-based boundary conditions of numerical simulations and

sampling designs for regional mesoscale and submesoscale circulation studies.

Disclosure statement

No potential conflict of interest was reported by the authors.

Funding

Eun Ae Lee and Sung Yong Kim are supported by grants through Basic Science Research Program through the National Research Foundation (NRF), Ministry of Education (NRF-2017R1D1A1B03028285) and Ministry of Oceans and Fisheries, and the Disaster and Safety Management Institute, Ministry of Public Safety and Security (KCG-01-2017-05), Republic of Korea. Hong Sik Min is supported by an in-house grant from the Korea Institute of Ocean Science and Technology (PE99711). This work forms a part of the graduate studies of the first author. The CTD data are provided by the National Institute of Fisheries Science / Korea Oceanographic Data Center (NIFS/KODC). More detailed regional currents around the Korean Peninsula can be found in Korea Hydrographic and Oceanographic Agency (https://www.khoa.go.kr/koofs/). The regressed climatology data are published as a Digital Object Identifier doi:l10.5281/zenodo.1751419. Sung Yong Kim contributed to this paper while being members of the Advisory Panel on North Pacific Coastal Ocean Observing Systems (AP-NPCOOS) and Working Group 38 (Mesoscale and Submesoscale Processes) of the North Pacific Marine Science Organization (PICES) and of the Boundary Currents and Shelf Sea Interactions (BC/SSI) in the Ocean Observations Physics and Climate (OOPC) Panel, Global Ocean Observing System (GOOS).

References

Abraham, J. P., Baringer, M., Bindoff, N. L., Boyer, T., Cheng, L. J. and co-authors. 2013. A review of global ocean temperature observations: Implications for ocean heat content estimates and climate change. *Rev. Geophys.* **51**, 450–483. doi:10.1002/rog.20022

Byun, S.-K. and Chang, S.-D. 1984. Two branches of Tsushima Warm Current in the western channel of the Korea Strait. *J. Oceanol. Soc. Korea* **19**, 200–209.

Cardin, V., Bensi, M. and Gačić, M. 2010. Deep ocean observing system over middle and long time scale: the E2M3A site in the Southern Adriatic.. In: *Proceedings of OceanObs'09: Sustained Ocean Observations and Information for Society (Annex)* (Hall, J., Harrison, D.E., Stammer, D. Eds.), ESA Publication, Venice, Italy.

Castelao, R., Glenn, S. and Schofield, O. 2010. Temperature, salinity, and density variability in the central Middle Atlantic Bight. *J. Geophys. Res.* **115**, C10005. doi:10.1029/2009JC006082

Chang, K.-I., Hogg, N. G., Suk, M.-S., Byun, S.-K., Kim, Y.-G. and Kim, K. 2002a. Mean flow and variability in the southwestern East Sea. *Deep-Sea Res. II* **49**, 2261–2279. doi:10.1016/S0967-0637(02)00120-6

Chang, K.-I., Kim, Y.-B., Suk, M.-S. and Byun, S.-K. 2002b. Hydrography around Dokdo. *Ocean Polar Res.* **24**, 369–389. doi:10.4217/OPR.2002.24.4.369

Chang, K.-I., Teague, W. J., Lyu, S. J., Perkins, H. T., Lee, D.-K. and co-authors. 2004. Circulation and currents in the southwestern East/Japan Sea: overview and review. *Prog. Oceanogr.* **61**, 105–156. doi:10.1016/j.pocean.2004.06.005

Chang, K.-I., Zhang, C.-I., Park, D.-J., Kang, S.-J., Ju, S.-H. and co-authors. 2015. *Oceanography of the East Sea (Japan Sea)*. Springer, Switzerland.

Cho, K.-D., Bang, T.-J., Shim, T.-B. and Yu, H.-S. 1990. Three dimensional structure of the Ullung Warm Lens, *Bull. Korean Fish. Soc.* **23**, 323–333.

Cho, Y. K. and Kim, K. 1996. Seasonal variation of the East Korea Warm Current and its relation with the cold water. *La Mer* **34**, 103–113.

Gordon, A. L., Giulivi, C. F., Lee, C. M., Furey, H. H., Bower, A. and Talley, L. 2002. Japan/East Sea intrathermocline eddies. *J. Phys. Oceanogr.* **32**, 1960–1974. 032⟨1960:JESIE⟩2.0.CO;2. doi:10.1175/1520-0485(2002)032<1960:JESIE>2.0.CO;2

Gouretski, V. and Koltermann, K. 2004. *WOCE Global Hydrographic Climatology*. Technical Report, Berichte des Bundesamtes fur Seeschifffahrt und Hydrographie.

Hartmann, D. L. 1994. *Global Physical Climatology, International Geophysics Series*, vol. 56, 411 pp., Academic Press, San Diego.

Hirose, N., Kim, C.-H. and Yoon, J.-H. 1996. Heat budget in the Japan Sea. *J. Oceanogr.* **52**, 553–574. doi:10.1007/BF02238321

Hogan, P. J. and Hurlburt, H. E. 2006. Why do intrathermocline eddies form in the Japan/East Sea? A modeling perspective. *Oceanography* **19**, 134–143. doi:10.5670/oceanog.2006.50

Hu, D.-X., Cui, M.-C., Li, Y.-X. and Qu, T.-D. 1991. On the Yellow Sea cold water mass-related circulation. *Yellow Sea Res.* **4**, 79–88.

Hwang, J. H., Van, S. P., Choi, B.-J., Chang, Y. S. and Kim, Y. H. 2014. The physical processes in the Yellow Sea. *Ocean Coast. Manage.* **102**, 449–457. doi:10.1016/j.ocecoaman.2014.03.026

Jeong, H.-D., Kim, S.-W., Lim, J.-W., Choi, Y.-K. and Park, J.-H. 2013. Time-series variation of sea surface salinity in the Southwestern East Sea. *Sea J. Korean Soc. Oceanogr.* **18**, 163–177.

Jeong, H.-D., Kwoun, C.-H., Kim, S.-W. and Cho, K.-D. 2009. Fluctuation of tidal front and expansion of cold water region in the Southwestern Sea of Korea. *J. Korean Soc. Mar. Environ. Saf.* **15**, 289–296.

Kang, Y. Q. and Jin, M. S. 1984a. Annual variation of salinity in the neighboring Seas of Korea. *J. Oceanol. Soc. Korea* **19**, 105–110.

Kang, Y. Q. and Jin, M. S. 1984b. Seasonal variation of surface temperature in the neighboring Seas of Korea. *J. Oceanol. Soc. Korea* **19**, 31–35.

Kim, C. H. and Kim, K. 1983. Characteristics and origin of the cold water mass along the East coast of Korea. *J. Oceanol. Soc. Korea* **18**, 73–83.

Kim, C. K., Chang, K. I., Park, K. and Suk, M. S. 2000. The South Sea circulation of Korea: two-dimensional barotropic model. *Sea J. Korean Soc. Oceanogr.* **5**, 226–257.

Kim, K. and Chung, J. 1984. On the salinity-minimum and dissolved oxygen-maximum layer in the East Sea (Sea of Japan). *Ocean Hydrodyn. Japan East China Seas* **39**, 55–65. doi:10.1016/S0422-9894(08)70290-3

Kim, K., Cho, Y.-K., Choi, B.-J., Kim, Y.-G. and Beardsley, R. C. 2002. Sea level variability at Ulleung island in the East (Japan) Sea. *J. Geophys. Res.* **107**. doi: 10.1029/2001JC000895.

Kim, K., Kim, K.-R., Min, D.-H., Volkov, Y., Yoon, J.-H. and co-authors. 2001. Warming and structural changes in the East (Japan) Sea: a clue to future changes in global oceans? *Geophys. Res. Lett.* **28**, 3293–3296. doi:10.1029/2001GL013078

Kim, K. Y., North, G. R. and Huang, J. 1996. EOFs of one-dimensional cyclostationary time series: computations, examples, and stochastic modeling. *J. Atmos. Sci.* **53**, 1007–1017. doi: 10.1175/1520-0469(1996)053<1007:EOODCT>2.0.CO;2

Kim, S. Y. 2014. A statistical description on the wind-coherent responses of sea surface heights off the U.S. West Coast. *Ocean Dyn.* **64**, 29–46. doi:10.1007/s10236-013-0668-3

Kim, S. Y. and Cornuelle, B. D. 2015. Coastal ocean climatology of temperature and salinity off the Southern California Bight: seasonal variability, climate index correlation, and linear trend. *Prog. Oceanogr.* **138**, 136–157. doi:10.1016/j.pocean.2015.08.001

Kim, Y.-G. and Kim, K. 1999. Intermediate waters in the East/Japan Sea. *J. Oceanogr.* **55**, 123–132. doi:10.1023/A:1007877610531

Kim, Y. H., Chang, K.-I., Park, J. J., Park, S. K., Lee and co-authors. 2009. Comparison between a reanalyzed product by 3-dimensional variational assimilation technique and observations in the Ulleung Basin of the East/Japan Sea. *J. Marine Syst.* **78**, 249–264. doi:10.1016/j.jmarsys.2009.02.017

Kim, Y. H. and Min, H. S. 2008. Seasonal and interannual variability of the North Korean Cold Current in the East Sea reanalysis data. *Ocean Polar Res.* **30**, 21–31. 1.021. doi: 10.4217/OPR.2008.30.1.021

Lee, C. M., Thomas, L. N. and Yoshikawa, Y. 2006. Intermediate water formation at the Japan/East Sea subpolar front. *Oceanography* **19**, 110–121.

Lee, E. A. and Kim, S. Y. 2018. Regional variability and turbulent characteristics of the satellite-sensed submesoscale surface chlorophyll concentrations. *J. Geophys. Res. Oceans* **123**, 4250–4279. doi:10.1029/2017JC013732

Lee, J.-S., Suh, Y.-S., Go, W.-J., Hwang, J.-D., Youn, S.-H. and co-authors. 2010. Improvement plan of NFRDI Serial Oceanographic Observation (NSO) system for operational oceanographic system. *J. Korean Soc. Mar. Environ. Saf.* **16**, 249–258.

Levitus, S., Boyer, T., Conkright, M., O'Brian, T., Antonov, J. and co-authors. 1998. *World Ocean Database NOAA Atlas NESDID 18*, Technical Report, US Government Printing Office, Washington, DC.

Lie, H. J. 1984. A note on water masses an general circulation in the Yellow Sea (Hwanghae). *J. Oceanol. Soc. Korea* **19**, 187–194.

Lie, H.-J. 1989. Tidal fronts in the southeastern Hwanghae (Yellow Sea). *Cont. Shelf Res.* **9**, 527–546. doi:10.1016/0278-4343(89)90019-8

Lie, H.-J. and Byun, S.-K. 1985. Summertime southward current along the East Coast of Korea. *J. Oceanol. Soc. Korea* **20**, 22–27.

Lie, H.-J., Cho, C.-H. and Jung, K. T. 2015. Occurrence of large temperature inversion in the thermohaline frontal zone at the Yellow Sea entrance in winter and its relation to advection. *J. Geophys. Res. Oceans* **120**, 417–435. doi:10.1002/2014JC010653

Lie, H.-J., Cho, C.-H., Lee, J.-H., Lee, S., Tang Y. and co-authors. 2001. Does the Yellow Sea Warm Current really exist as a persistent mean flow? *J. Geophys. Res.* **106**, 22,199–22,210. doi:10.1029/2000JC000629

Lim, S., Jang, C. J., Oh, I. S. and Park, J. 2012. Climatology of the mixed layer depth in the East/Japan Sea. *J. Marine Syst.* **96**, 1–14.

Luyten, J., McCartney, M., Stommel, H., Dickson, R. and Gmitrowicz, E. 1993. On the Sources of North Atlantic Deep Water. *J. Phys. Oceanogr.* **23**, 1885–1892. doi:10.1175/1520-0485(1993)023<1885:OTSONA>2.0.CO;2

Lynn, R. J. and Simpson, J. J. 1987. The California current system: the seasonal variability of its physical characteristics. *J. Geophys. Res.* **92**, 12,947–12,966. doi:10.1029/JC092iC12p12947

Min, H. S., Kim, Y.-H. and Kim, C.-H. 2006. Year-to-year variation of cold waters around the Korea Strait. *Ocean Sci. J.* **41**, 227–234. doi:10.1007/BF03020626

Mitchell, D., Watts, D., Wimbush, M., Teague, W., Tracey, K. and co-authors. 2005. Upper circulation patterns in the Ulleung Basin. *Deep-Sea Res. II* **52**, 1617–1638. doi:10.1016/j.dsr2.2003.09.005

Moon, J.-H., Hirose, N. and Yoon, J.-H. 2009. Comparison of wind and tidal contributions to seasonal circulation of the Yellow Sea. *J. Geophys. Res.* **114**. doi: 10.1029/2009JC005314.

Morimoto, A., Yanagi, T. and Kaneko, A. 2000. Eddy field in the Japan Sea derived from satellite altimetric data. *J. Oceanogr.* **56**, 449–462. doi:10.1023/A:1011184523983

Na, J.-Y., Han, S.-K. and Cho, K.-D. 1990. A study on sea water and ocean current in the sea adjacent to Korea Peninsula: Expansion of coastal waters and its effect on temperature variations in the South Sea of Korea. *Korean J. Fish. Aquat. Sci.* **15**, 289–296.

Pang, I.-C., Hong, C. S., Chang, K. I., Lee, J. C. and Kim, J. T. 2003. Monthly variation of water mass distribution and current in the Cheju Strait. *Sea J. Korean Soc. Oceanogr.* **38**, 87–100.

Park, S. and Chu, P. C. 2006. Thermal and haline fronts in the Yellow/East China Seas: surface and subsurface seasonality comparison. *J. Oceanogr.* **62**, 617–638. doi:10.1007/s10872-006-0081-3

Pond, S. and Pickard, G. 1983. *Introductory Dynamical Oceanography*. 2nd ed. Butterworth-Heinemann, Oxford.

Qiu, B., Chen, S., Klein, P., Sasaki, H. and Sasai, Y. 2014. Seasonal mesoscale and submesoscale eddy variability along the North Pacific Subtropical Countercurrent. *J. Phys. Oceanogr.* **44**, 3079–3098. doi:10.1175/JPO-D-14-0071.1

Roemmich, D. and Gilson, J. 2009. The 2004-2008 mean and annual cycle of temperature, salinity, and steric height in the global ocean from the Argo Program. *Prog. Oceanogr.* **82**, 81–100. doi:10.1016/j.pocean.2009.03.004

Rudnick, D. L. and Ferrari, R. 1999. Compensation of horizontal temperature and salinity gradients in the ocean mixed layer. *Science* **283**, 526–529. doi:10.1126/science.283.5401.526

Schaeffer, A., Roughan, M., Austin, T., Everett, J. D., Griffin, D. and co-authors. 2016. Mean hydrography on the continental shelf from 26 repeat glider deployments along Southeastern Australia. *Sci. Data* **3**, 160070. doi:10.1038/sdata.2016.70

Shin, H.-R., Byun, S.-J., Kim, C.-S., Hwang, S.-C. and Shin, C.-W. 1995. The characteristics of structure of Warm Eddy observed to the northwest of Ullungdo in 1992. *J. Oceanol. Soc. Korea* **30**, 39–56.

Shin, H.-R., Shin, C.-W., Kim, C., Byun, S.-K. and Hwang, S.-C. 2005. Movement and structural variation of warm eddy for three years in the western East/Japan Sea. *Deep-Sea Res. II* **52**, 1742–1762. doi:10.1016/j.dsr2.2004.10.004

Soh, H. S. and Kim, S. Y. 2018. Diagnostic characteristics of submesoscale coastal surface currents. *J. Geophys. Res. Oceans* **123**, 1838–1859. doi:10.1002/2017JC013428

Son, Y. T., Lee, S. H., Choi, B. J. and Lee, J. C. 2010. Frontal structure and thermohaline intrusions in the South Sea of Korea from observed data and a relocation method. *J. Geophys. Res.* **115**, C02011.

Stommel, H. 1962. On the cause of the temperature-salinity curve in the ocean. *Proc. Natl. Acad. Sci. USA* **48**, 764–766. doi:10.1073/pnas.48.5.764

Talley, L. D., Luchin, V. A., Ponomarev, V. I., Salyuk, A. N., Shcherbina, A. Y. and co-authors. 2006. Water masses. *Oceanography* **19**, 32–49. doi:10.5670/oceanog.2006.42

Turner, J. and Stommel, H. 1964. A new case of convection in the presence of combined vertical salinity and temperature gradients. *Proc. Natl. Acad. Sci. USA* **52**, 49–53. doi:10.1073/pnas.52.1.49

Veronis, G. 1972. On properties of sea water defined by temperature, salinity and pressure. *J. Mar. Res.* **30**, 227–255.

Wang, B., Hirose, N., Kang, B. and Takayama, K. 2014. Seasonal migration of the Yellow Sea Bottom Cold Water. *J. Geophys. Res. Oceans* **119**, 4430–4443. doi:10.1002/2014JC009873

WOCE International Project Office 2003. *WOCE Observations 1990-1998: A Summary of the WOCE Global Data Resource*. Technical Report, WOCE Report No. 179/02, WOCE International Project Office, Southampton, UK.

Wong, A. P., Johnson, G. C. and Owens, W. B. 2003. Delayed-mode calibration of autonomous CTD profiling float salinity data by θ-S climatology. *J. Atmos. Oceanic Technol.* **20**, 308–318. DMCOAC⟩2.0.CO;2. doi:10.1175/1520-0426(2003)020<0308:DMCOAC>2.0.CO;2

Yang, Y. J., Kim, S. H. and Rho, H. K. 1998. A study on the temperature fronts observed in the South-West Sea of Korea and the northern area of the East China Sea. *Korean J. Fish Aquat. Sci.* **31**, 695–706.

Yoo, J. G., Kim, S. Y. and Kim, H. S. 2018. Spectral descriptions of submesoscale surface circulation in a coastal region. *J. Geophys. Res. Oceans* **123**, 4224–4249. doi:10.1029/2016JC012517

Yoon, J.-H., Abe, K., Ogata, T. and Wakamatsu, Y. 2005. The effects of wind-stress curl on the Japan/East Sea circulation. *Deep-Sea Res. II* **52**, 1827–1844. doi:10.1016/j.dsr2.2004.03.004

Yoon, S.-T., Chang, K.-I., Na, H. and Minobe, S. 2016. An east-west contrast of upper ocean heat content variation south of the subpolar front in the East/Japan Sea. *J. Geophys. Res. Oceans* **121**, 6418–6443. doi:10.1002/2016JC011891

Yoshikawa, Y., Awaji, T. and Akitomo, K. 1999. Formation and circulation processes of intermediate water in the Japan Sea. *J. Phys. Oceanogr.* **29**, 1701–1722. doi:10.1175/1520-0485(1999)029<1701:FACPOI>2.0.CO;2

Yoshikawa, Y., Lee, C. M. and Thomas, L. N. 2012. The subpolar front of the Japan/East Sea. Part III: competing roles of frontal dynamics and atmospheric forcing in driving ageostrophic vertical circulation and subduction. *J. Phys. Oceanogr.* **42**, 991–1011. doi:10.1175/JPO-D-11-0154.1

Yun, J. Y., Magaard, L., Kim, K., Shin, C. W., Kim, C. and co-authors. 2004. Spatial and temporal variability of the North Korean Cold Water leading to the near-bottom cold water intrusion in Korea Strait. *Prog. Oceanogr.* **60**, 99–131. doi:10.1016/j.pocean.2003.11.004

Zhang, S., Wang, Q., Lu, Y., Cui, H. and Yuan, Y. 2008. Observation of the seasonal evolution of the Yellow Sea Cold Water Mass in 1996–1998. *Cont. Shelf Res.* **28**, 442–457. 2007.10.002. doi:10.1016/j.csr.2007.10.002

Appendix A. Uncertainty of the regression analysis

Since the temperature and salinity profiles are obtained from in-situ CTD casts, the time series at a single station and depth may have missing data. Additionally, the time records of the entire data set may not have concurrent time stamps. Thus, the time series have irregular time intervals and mismatched time stamps across both stations and lines. The signal-to-noise ratio (SNR) and the uncertainty of the proposed regression analysis should be quantified to assure confidence in the regression results. Thus, we quantify the error of the regression analysis by accounting for how well an assumed time series with annual variance and noise is reconstructed. Therefore, a 20-year time series (d) with a pure annual variance signal (s in Equation A1), random noise (ϵ in Equation A1) having a given SNR (p in Equation A4) is generated as true data,

$$d(t) = s(t) + \epsilon(t), \tag{A1}$$

$$= a\sin(\sigma t) + \epsilon(t), \tag{A2}$$

where a is the amplitude of the signal [$\sigma = 2\pi/365.2425$ rpd]. A sample time series [$\tilde{d} = d(\tilde{t})$] is created by resampling the true data at the time stamps ($\tilde{t}$) with identical statistics to the time stamps of the in-situ CTD data:

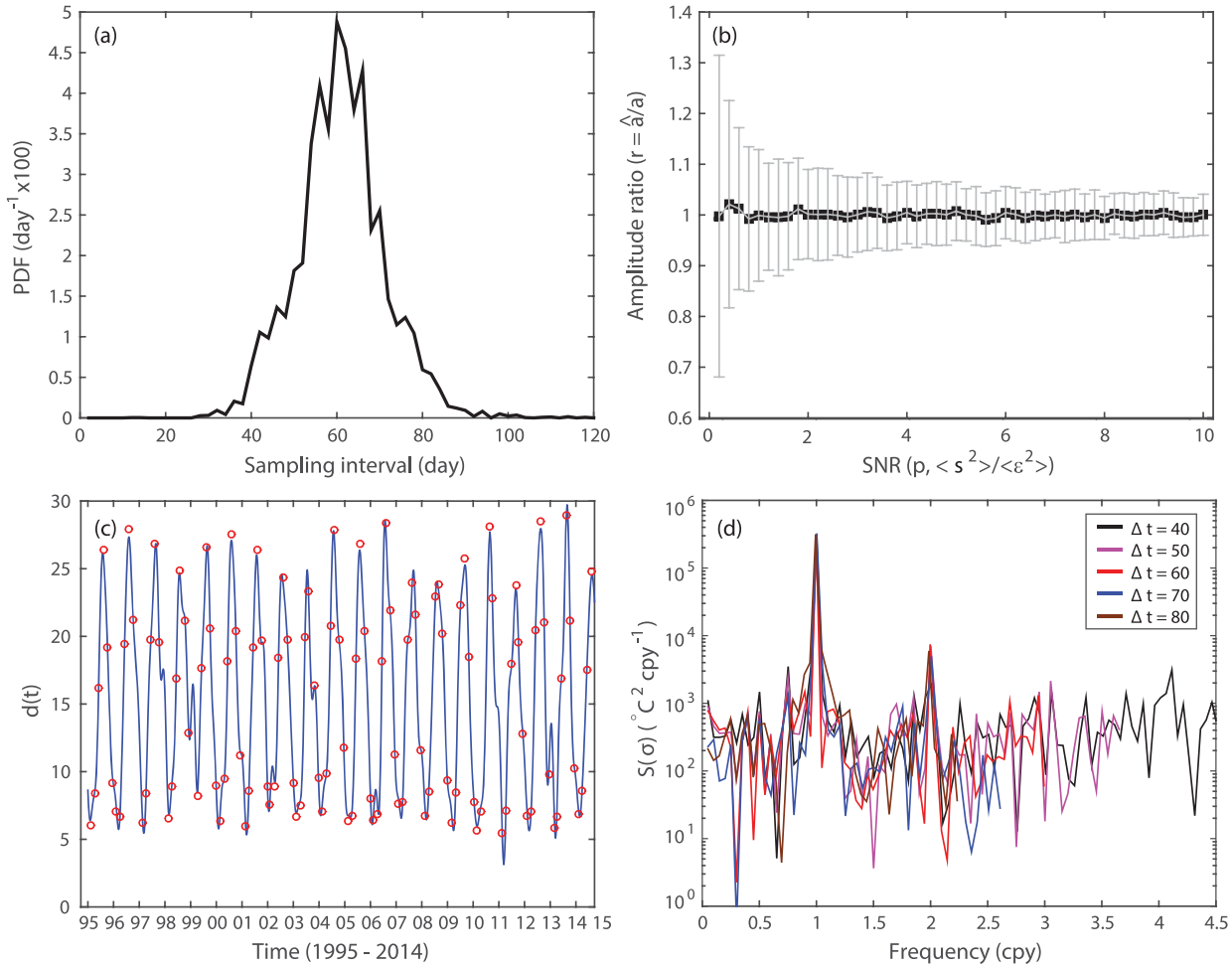

Fig. A1. (a) A PDF of sampling intervals obtained from the CTD data for a period of recent 20 years (1995 to 2014). (b) Ensemble mean of ratios ($r = \langle \hat{a}/a \rangle$) of the estimated amplitude ($\hat{a}$) to true amplitude (a in Equation A2) is presented as a function of SNR ($p = \langle s^2(t) \rangle / \langle \epsilon^2(t) \rangle$) in Equation A4). (c) Reconstructed temperature time series (blue) and sampled data (red circles) at the Line 307, station 10, and 0 m depth when the time axis is defined with $\Delta t = 50$ days. (d) Energy spectra of reconstructed temperature time series using the slow FFT method are presented as a function of constant time intervals ($\Delta t = 40$, 50, 60, 70, and 80 days). The noise floor level is equal to 1.78°C, and the frequency axis is given as cycles per year (cpy).

$$d(\tilde{t}) = a \sin(\sigma \tilde{t}) + \epsilon(\tilde{t}). \tag{A3}$$

The SNR can be defined as

$$p = \frac{\langle s^2(t) \rangle}{\langle \epsilon^2(t) \rangle}, \tag{A4}$$

where $\langle \cdot \rangle$ indicates the ensemble mean.

To increase the degrees of freedom in the error estimate, the time axis (t) is composed of a random combination of the cumulative sum of the time intervals:

$$t(k) = \sum_{j=1}^{k} \Delta t(j), t \leq L, \tag{A5}$$

where L denotes the maximum length of the time series ($L = 20$ years). The time axes are generated by randomly shuffling the order of the sampling time intervals (Δt) and maintaining the same PDF of the sampling intervals, which follows Gaussian statistics. The mean and standard deviation of the time axes are estimated as 61.4 days and 11.8 days, respectively (Fig. A1a). A set of 200 independent observations (M) is chosen, and the ensemble mean of ratios ($r = \langle \hat{a}/a \rangle$) of the estimated amplitudes to true amplitudes is presented as a function of the SNR (Fig. A1b). The regression errors decrease with higher SNR.

The Fourier coefficients of the irregularly sampled temperature time series at the surface ($z = 0$ m) in the station 10 on the Line 307 are estimated using the slow finite Fourier transform method, which is a least-squares fit using all orthogonal basis functions (all available frequencies) (Fig. A1c) (Kim, 2014; Soh and Kim, 2018).

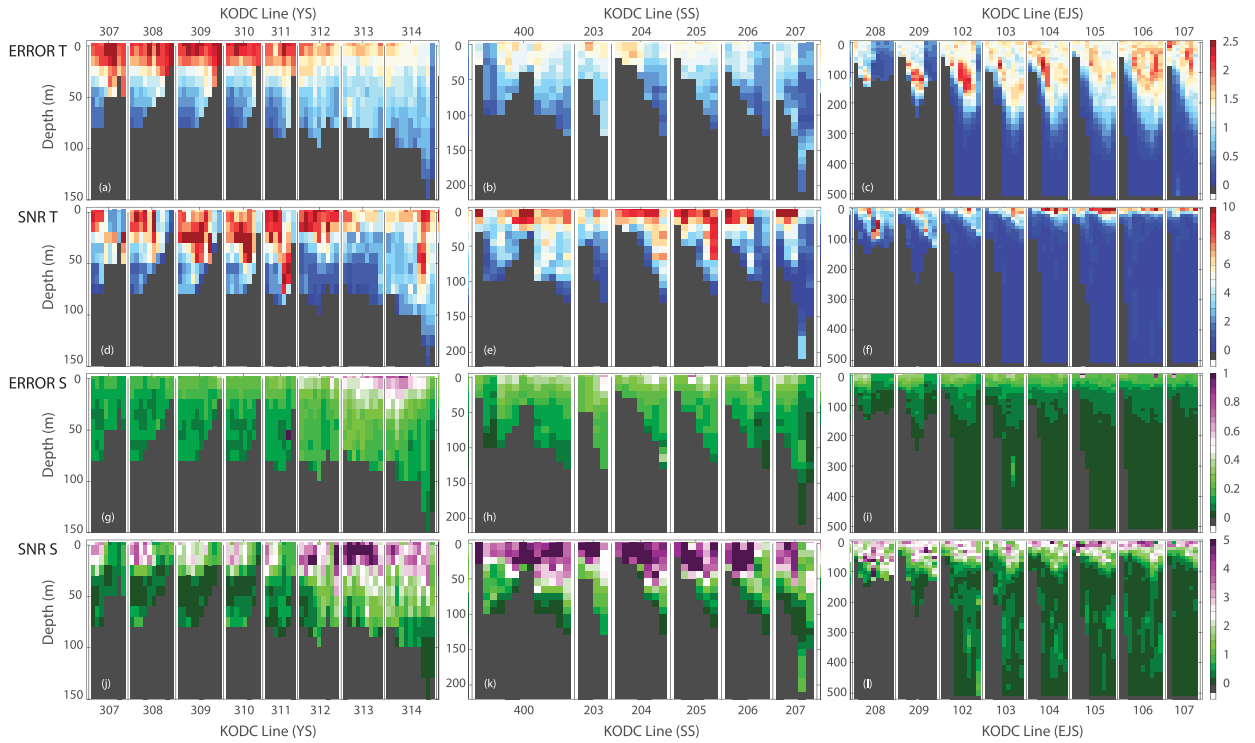

Fig. A2. Zonal sections of the observational noise (ϵ) and SNR (p) of the temperature (°C) and salinity profiles at the annual frequency (SA_1) sampled in the YS, SS, and EJS for a period of recent 20 years (1995 to 2014). (a–c) Observational noise (ϵ) of the temperature at the annual frequency. (d–f) SNR (p) of the temperature at the annual frequency. (g–i) Observational noise (ϵ) of the salinity at the annual frequency. (j–l) SNR (p) of the salinity at the annual frequency. (a), (d), (g), and (j): YS. (b), (e), (h), and (k): SS. (c), (f), (i), and (l): EJS. The vertical profiles are concatenated in terms of cross-shore lines, and the unsampled depths and bottom bathymetry are shown as gray columns.

Four cases of constant time intervals (Δt = 40, 50, 60, 70, and 80 days) are considered, and the energy spectra obtained from the estimated Fourier coefficients using corresponding time axes show consistent peaks at annual and semi-annual frequencies with a noise level that is nearly flat and of a similar order of magnitude (Fig. A1d). Thus, we can utilize the noise level for the SNR of the annual cycle.

This approach is applied to the temperature and salinity time series at all stations and depths. The observational errors are less than 2.5°C and 0.7, respectively, and vary with the region (e.g. YS, EJS, and SS), a distance from shore, and the depth (Figs. A2a–A2f). At the annual frequency, the SNR of the temperature in the upper ocean (less than 100 m depth) is higher than the subsurface temperature (below 100 m depth). Additionally, the SNR of the salinity becomes significant in the SS. Based on the SNR, we can determine an effective depth where the annual amplitude becomes meaningful (Figs. A2g–A2l and 4). A similar method is used to quantify the observational errors and SNR of the temperature and salinity at the semi-annual frequency as less than 0.3°C and 0.1, respectively (not shown).

Appendix B. Implementation of the inverse method

In this paper, the inverse method is formulated as a weighted least-squares fit, and the estimated model coefficients are,

$$\hat{\mathbf{m}} = \mathbf{P}\mathbf{G}^{\dagger}(\mathbf{G}\mathbf{P}\mathbf{G}^{\dagger} + \mathbf{R})^{-1}(\mathbf{d} - \langle \mathbf{d} \rangle), \tag{B1}$$

where $\mathbf{P}$ and $\mathbf{R}$ denote the model covariance matrix and the noise covariance matrix of the sampled data, respectively.

The model covariance matrix ($\mathbf{P}$) is assumed to be a diagonal matrix with an assumption of uncorrelated amplitudes of the basis functions,

$$\mathbf{P} = \begin{bmatrix} \mathbf{P}_S & 0 \\ 0 & \mathbf{P}_F \end{bmatrix}. \tag{B2}$$

The individual prior terms ($\mathbf{P}_S$ and $\mathbf{P}_F$) in the model covariance matrix are assumed to have equal unit

variance. For instance, the prior ($\mathbf{P}_S$) for annual and semi-annual components has an exponentially decaying variance at the higher harmonics, which is observed in the natural resonance of geophysical signals (e.g. variance of the diurnal wind and its harmonics) (see Kim and Cornuelle (2015) for more details).

The error covariance matrix ($\mathbf{R}$) is assumed to be a scaled diagonal matrix with an assumption of uncorrelated noise between corresponding to basis functions,

$$\mathbf{R} = \alpha^2 \mathbf{I}, \tag{B3}$$

where α^2 denote the noise variance of the error covariance matrix. Although the choice of the model and error covariance matrices can affect the estimates of regression coefficients, its role is negligible in this study because the variance of data corresponding to the basis functions is significant compared with the noise level.

Appendix C. Annual variance modulated by low-frequency variance

The variance associated with the linear trend and the annual cycle can be expressed as a slowly varying annual variance or a summation depending on the degree of modulation of the two signals. This issue has been discussed in the context of the amount of variance spread at the annual frequency (SA_1) (Kim and Cornuelle, 2015). Three time series with variance of the linear sum (d_1), linear product (d_2), and cosine product (d_3) of the linear trend and annual variance are examined (Fig. C1a).

$$d_1(t) = \frac{t - \langle t \rangle}{\max(t) - \min(t)} + g(t), \tag{C1}$$

$$d_2(t) = [t - \min(t)]g(t), \tag{C2}$$

$$d_3(t) = \left(\cos\frac{\sigma t}{50}\right)g(t), \tag{C3}$$

where

$$g(t) = \cos\sigma t + \sin\sigma t + \frac{1}{10}\cos 2\sigma t + \frac{1}{5}\sin 2\sigma t, \tag{C4}$$

$\sigma = 2\pi/365.2425$ rpd is the annual frequency, and $\langle t \rangle$ is the center of the time axis.

The energy spectra of the individual time series are shown in Fig. C1b. The time series of the linear sum contains the red spectrum and sharp peaks at the annual and semi-annual frequencies. However, the linear product and slowly varying signals exhibit wider peaks at the annual and semi-annual frequencies, indicating the modulation of annual variance.

Appendix D. Total skill and standard deviations of residuals

The total skill denotes how much variance is explained by the regression (Figs. D1a-D1e and D1g-D1i), defined as

$$\kappa = 1 - \frac{\langle \mathbf{d}_R^2(t) \rangle}{\langle \mathbf{d}^2(t) \rangle}, \tag{D1}$$

and the standard deviations of residuals $[\langle \mathbf{d}_R^2(t) \rangle^{1/2}]$ show how much variance remains in the data (Figs. D1d-D1f and D1j-D1l).

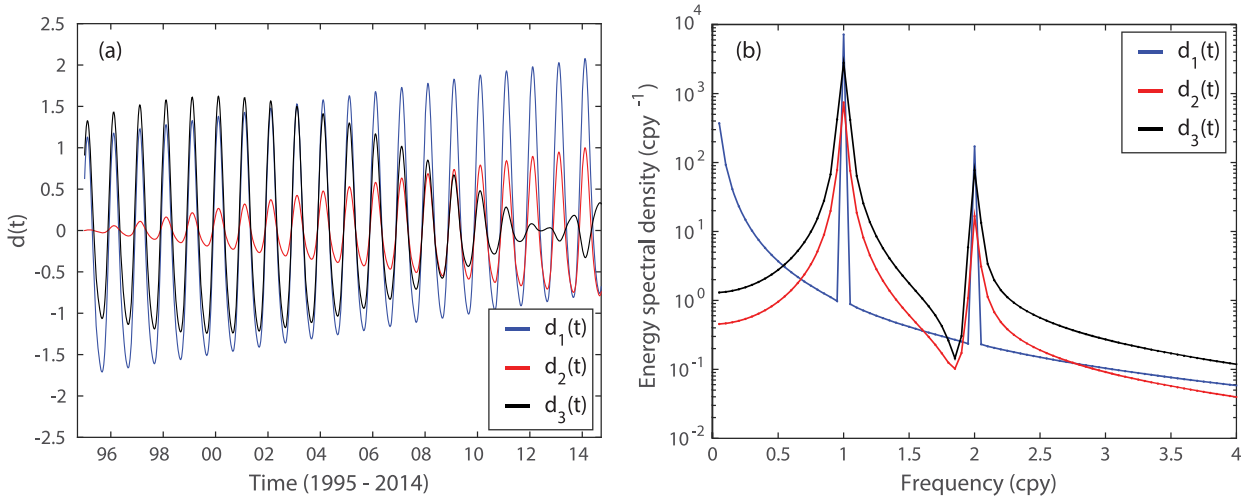

Fig. C1. (a) Examples of time series modulated with linear sum [$d_1(t)$], linear product [$d_2(t)$], and cosine product [$d_3(t)$] with annual and semi-annual signals time series [$g(t)$ in Equation C4] and (b) their energy spectral density.

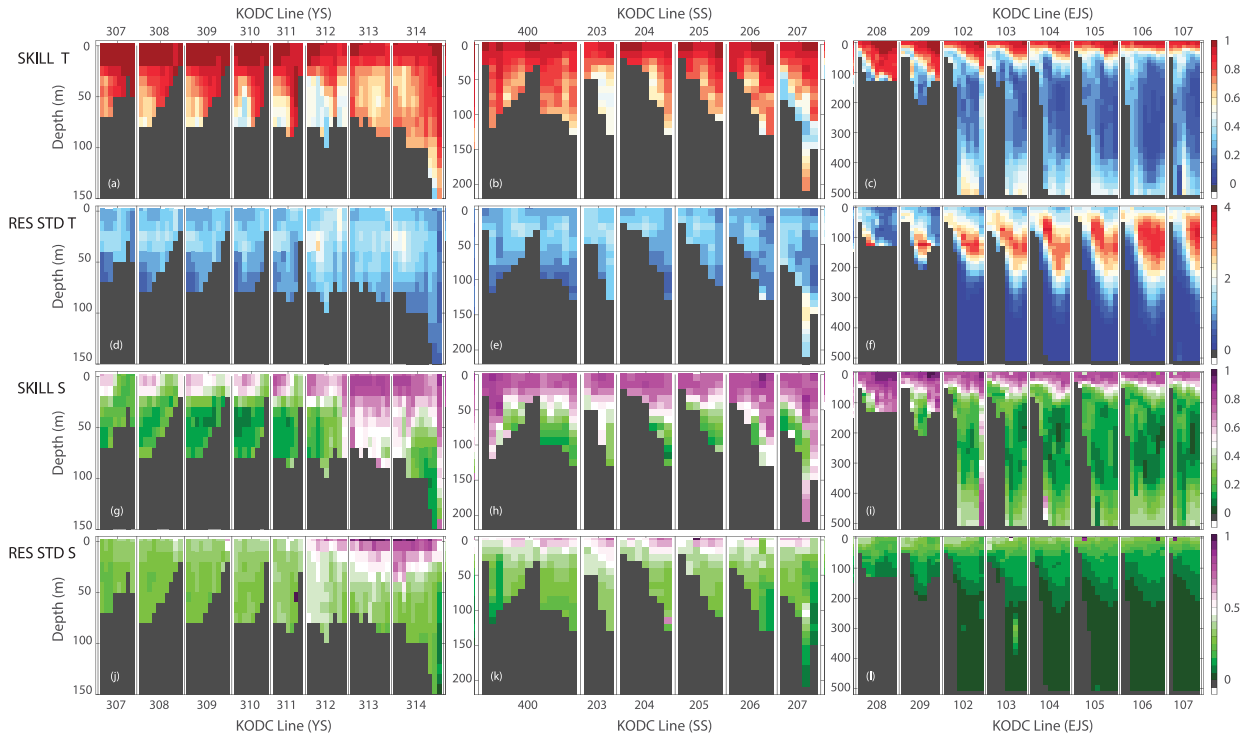

Fig. D1. Zonal sections of the total skill (κ) and standard deviation ($\langle \mathbf{d}_R^2(t) \rangle^{1/2}$) of the residual temperature (°C) and salinity profiles sampled in the YS, SS, and EJS for a period of recent 20 years (1995 to 2014). (a–c) Total skill (κ) of the temperature. (d–f) Standard deviation ($\langle \mathbf{d}_R^2(t) \rangle^{1/2}$) of the residual temperature. (g–i) Total skill (κ) of the salinity. (j–l) Standard deviation ($\langle \mathbf{d}_R^2(t) \rangle^{1/2}$) of the residual salinity. (a), (d), (g), and (j): YS. (b), (e), (h), and (k): SS. (c), (f), (i), and (l): EJS. The vertical profiles are concatenated in terms of cross-shore lines, and the unsampled depths and bottom bathymetry are shown as gray columns.